TAIVO JÕGIAAS

Mechanical properties of atomic layer
deposited thin films and nanocomposites

DISSERTATIONES SCIENTIAE MATERIALIS UNIVERSITATES TARTUENSIS

21

TAIVO JÕGIAAS

Mechanical properties of atomic layer deposited thin films and nanocomposites

The study was carried out at Institute of Physics, University of Tartu, Estonia.

The dissertation was submitted on 29.06.2017 to fill the requirements for degree of Doctor of Philosophy in Materials Science, and was allowed for defense by the Scientific Council on Materials Science of the University of Tartu.

Supervisors: Research professor Kaupo Kukli (PhD), Institute of Physics, University of Tartu, Tartu, Estonia.

Senior research fellow Aile Tamm (PhD), Institute of Physics, University of Tartu, Tartu, Estonia.

Professor Irina Hussainova (PhD), Department of Mechanical and Industrial Engineering, Tallinn University of Technology, Tallinn, Estonia.

Opponents: Prof. Riika Puurunen, Department of Chemical and Metallurgical Engineering, University of Aalto, Finland.

Tõnu Leemet (PhD), researcher, Institute of Technology, Estonian University of Life Sciences, Estonia.

Defense: August 24th, 2017 at university of Tartu, Estonia.

European Union
European Regional
Development Fund

Investing
in your future

TABLE OF CONTENTS

LIST OF ORIGINAL PUBLICATIONS AND AUTHOR'S CONTRIBUTIONS

The present thesis is based on following original publications, referred in text with roman numerals I–IV:

I. T. Jõgiaas, T. Arroval, L. Kollo, J. Kozlova, T. Käämbre, H. Mändar, A. Tamm, I. Hussainova, K. Kukli. Atomic layer deposition of alumina on γ-alumina nanofibres. *Physica Status Solidi A* 211, No. 2, 403–408 (2014). DOI: 10.1002/pssa.201330083.

In this article the applicants part was organizing the work, carrying out atomic layer deposition on prepared thin nanofiber slices, measuring film thicknesses on references using spectroscopic ellipsometer, conducting μ-Raman measurements, analyzing the results and writing the manuscript.

II. T. Jõgiaas, L. Kollo, J. Kozlova, A. Tamm, I, Hussainova, K. Kukli. Effect of atomic layer deposited aluminium oxide on mechanical properties of porous silicon carbide. *Ceramics International* 41, 7519–7528 (2015). DOI: 10.1016/j.ceramint.2015.02.074.

In this article the applicant's part was creating the experimental plan, organizing the work, carrying it out using atomic layer deposition on compacted silicon carbide nanopowder substrates, measuring the film thicknesses on references using spectroscopic ellipsometer, measuring the mechanical properties of produced samples, analyzing the results and writing the manuscript.

III. T. Jõgiaas. R. Zabels, A. Tamm, M. Merisalu, I. Hussainova, M. Heikkilä, H. Mändar. K. Kukli, M. Ritala, M. Leskelä. Mechanical properties of aluminum, zirconium, hafnium and tantalum oxides and their nanolaminates grown by atomic layer deposition. *Surface&Coatings Technology* 282, 36–42 (2015). DOI: 10.1016/j.surfcoat.2015.10.008.

In this article the applicants part was organizing the work, analyzing the results and writing the manuscript.

IV. K. Kukli, E. Salmi, T. Jõgiaas, R. Zabels, M. Schuisky, J. Westlinder, K. Mizohata, M. Ritala, M. Leskelä. Atomic layer deposition of aluminum oxide on modified steel substrates. *Surface&Coatings Technology* 304, 1–8 (2016). DOI: 10.1016/j-surfcoat.2016.06.064.

In this article the applicants part was organizing the work, analyzing the results and partly writing the manuscript.

LIST OF ABBREVIATIONS

ALD – atomic layer deposition
CSM – continuous stiffness measurement
CVD – chemical vapor deposition
E – modulus of elasticity
E_r – reduced modulus
E_{tr} – true/absolute modulus
H – hardness
P-C – model of Puchi-Cabrera
ROM – rule of mixture
SEM – scanning electron microscope
SLG – soda-lime-glass
XRD – X-ray diffraction
XRF – X-ray fluorescence

THE CLAIM OF THE THESIS

The author of the thesis claims that atomic layer deposition can be used to produce nanostructured composite materials with relatively high hardness and modulus of elasticity.

Four original and published articles (denoted as I–IV) are presented to back up and discuss the claim.

INTRODUCTION

The current work was directed to create and characterize nanostructured composite hard coatings using atomic layer deposition (ALD) as the main technique. ALD allows to create structures with very thin film layers, even below 1 nm. The scientific reasoning for the research was driven by the fact that it is not clear how materials mechanically behave at such low scales or how the ALD thin films, separately or in composite structure, behave and can ALD to be used to produce nanostructured composites and what the mechanical properties would be. From the applications point of view, several materials with relatively high hardness and modulus were produced and described, which could be applied as mechanically protective coatings (for instance in micro- or nanoelectromechanical devices) from submicron to few microns in thickness.

Atomic layer deposition is a modification of chemical vapor deposition method with broad application areas [1]. During ALD, a thin film is deposited on a substrate layer-by-layer, therefore allowing very precise control over deposition (the film thickness etc.). By the selection of deposition conditions and precursors, the crystallinity of a deposit can be modified and changed from amorphous to some crystalline phase [2]. This can be employed as a method to produce highly controlled and tuned nanostructures with very different compositions and phases.

One of the first industrial applications of ALD was electroluminescent displays in 1980's and in micro- or nanoelectronics it is exploited also today [3–6]. Other application areas include, for instance, depositing catalytic, corrosion resistant or hard, mechanically protective thin films [7–9]. The latter one, *i. e.* the opening possibility to deposit very thin, but mechanically hard or elastic coatings, was selected as a starting point for this thesis.

To fulfill the thesis claim, the produced materials were characterized by means of measuring their structure hardness and modulus of elasticity. Although there are several methods to describe a material behavior and response under mechanical influences, an instrumented depth sensing nanoindentation technique was selected as a characterization method [10–12].

Composites represent a very interesting class of materials due to the fact that new versatile materials can be made by combining different materials [13]. For instance, epoxy bonded glass fiber composites have been widely used because the tensile properties would be superior to steels compared to its low density, despite the fact that glasses are brittle and epoxies are polymers, which both do not resemble to steels [14]. The materials, produced in this thesis, mostly possessed composite structure.

ATOMIC LAYER DEPOSITION

Atomic layer deposition is a chemical thin film deposition method, where successive precursor vapor pulses are used to deposit solids on a solid substrate [15–18]. The distinctive difference from a regular chemical vapor deposition is in its cyclic nature (Fig. 1). The first precursor is introduced in a reaction chamber followed by an inert gas purge pulse, which should leave only one monolayer of precursor molecules adsorbed (chemisorbed) on the substrate. The substrate should be saturated with precursor molecules as much as possible, although 100% coverage is usually not achieved. This means that several cycles are needed to gain one monolayer (or equivalent) thick solid deposit.

The second precursor is used in the same manner. The precursors would react, leaving a formed solid on top of the substrate. Any other volatile compounds, introduced and/or formed during the reaction, have to be evacuated from the reaction chamber during the second purge pulse. By starting the steps again from the first precursor, a layer by layer deposition is achieved.

## Deposition conditions and materials

The conditions of ALD can vary. It has been conducted at atmospheric pressure [19], but usually low vacuum in several millibar range is used [20]. The deposition temperatures can vary from room temperature to 800 °C, possibly even higher [21].

Probably the most frequently studied materials in ALD are oxides of various metals. Over the years (about three decades) oxides starting from those of magnesium and aluminum and ending with rare-earth metals have been deposited. The driving force here has been the ever increasing need for very good dielectric materials in electronic industry, which has led to several oxides with high permittivity constants (high-k materials). The later allows to reduce the size (down to several tens of nanometers or even less) of single units (transistors, capacitors) in electronics and therefore pack more and more computational power in a chip. ALD is very well suited for nanoelectronics because its deposition conformity and ability to build up a material layer-by-layer, thus allowing immense control over the deposited layer thickness.

The precursors for metal-ions for oxide deposition can be inorganic halide salts (*i. e.* chlorides, iodides, bromides) or metal-organic compounds (*i. e.* methoxides, ethoxides). Each precursor has its pros and cons. For instance, halides may require more heating to vaporize but can be more stable in time and do not go through pyrolysis during deposition at higher temperatures. Metal-organic compounds can be usually easily volatilized but tend to decompose at higher temperatures and the thin films composition could turn out to include some carbon or other elements, which an experimenter would rather exclude [22].

The oxygen source for ALD oxides has most often been distilled water, but purified oxygen, ozone or even nitrous oxides have been used as well [23,24]. Compared to other oxidizing agents, water is cheap, abundant, easy to store and use. Water has vapor pressure sufficiently high, *i. e.* not requiring extra heating upon vaporization, and is also sufficiently reactive at low temperatures towards many metal precursors common in ALD, such as chalcogenides (halides), alkoxides, alkylamides and alkyls.

In Figure 1, a schematic presentation of reaction between $ZrCl_4$ and H_2O during an ALD cycle is shown. The pulse times might vary and depend on used precursors and systems.
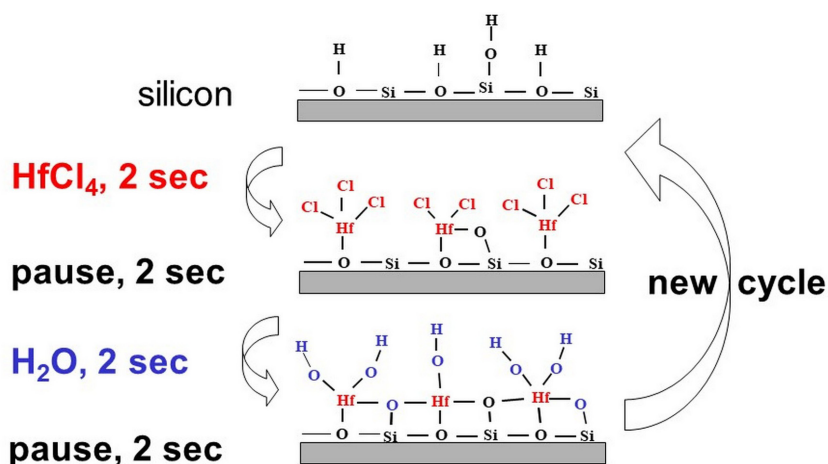
Figure 1. A simplified scheme of an ALD cycle describing the deposition of ZrO_2 from $ZrCl_4$ and H_2O as precursors with exemplified pulse timing 2/2/2/5 s.

Processes on solid-gas interfaces

The property of a gaseous material to adhere on a solid surface is called adsorption. The opposite phenomenon, detachment of adsorbed molecules into gaseous phase, is called desorption. For the effective, there has to be available/ free solid surface, where no molecules have not adsorbed yet and the molecule can fit in. The interaction between a surface and a molecule has to be strong enough to retain it on the surface (in other words, it must be energetically favored). Adsorption processes can be distinguished between physical adsorption (physisorption) or chemical adsorption (chemisorption).

Chemisorption is similar to the physisorption, but the main difference is that a chemical bond is formed between a molecule and the surface (or between a molecule and a previously adhered molecule). Therefore, to reverse chemisorption, an energy at least equal to the bond energy is required to brake the molecule loose from the surface. To put the energy levels on a scale, Table I was formed.

Table I. A comparison of bond strengths according earlier works [25,26].

Bond type	Bond energy, kJ/mol
Van der Waals	0.4–4.0
Hydrogen bonds	12–30
Ionic interactions	20
Chemical bond in solid oxides	1000–2000

In ALD processes, only chemical adsorption is utilized. Any physical adsorption could boost growth rate or interfere some other way with the pure ALD process. Usually the process parameters (for instance temperature, carrier gas flow rate) can be appropriately selected to avoid physisorption. The temperature should be selected to overcome the physisorption energies of a precursor molecules and the carrier gas molecules would remove the excess precursor from the surface and carry away.

During an ALD process a molecule could adsorb-desorb more than once before it could go through chemical reaction on the substrate. (This applies to any of the reaction products also.) Every adsorbed molecule might not form a chemical bond in the first adsorption process. This necessitates the reason why ALD precursors have to be chemically aggressive – the time for forming a chemical bond could be very short. An aggressive precursor would react fast on the first impact. But still, there might not be enough energy to overcome chemical reaction activation energy or the steric hindrance of molecules could interfere the process.

The adsorption of volatile reaction product molecules poses another threat to ALD process success. For instance, hydrogen chloride can form volatile products if it re-adsorbs on a thin film and these molecules could desorb from the substrate and create an etching effect, thus reducing the thin film growth rate. This kind of etching effect could be caused also by a precursor, $TaCl_5$ for instance [27,28].

The temperature dependence of adsorption and desorption rate constant k temperature dependence can be described by the Arrhenius equation:

$$k = A \times e^{-E_i/RT}$$
Equation 1

A is a pre-exponential factor, E_i is the process i activation energy, R is the gas constant and T is the absolute temperature. In a balanced situation the adsorption rate constant equals the desorption rate constant, meaning that the molecules adsorb as fast as they desorb. Arrhenius equation can be written for any adsorbing-desorbing species. The equation also expresses that the chemical reactions would accelerate at higher temperatures.

As for the bond formation on a substrate during ALD, three main mechanisms have been accepted: ligand exchange, dissociation and association (Fig. 2).

a) ligand exchange
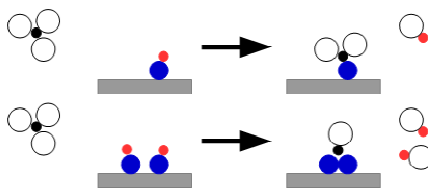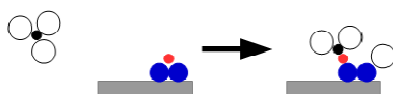
b) dissociation

c) association

Figure 2. Three possible chemical bond formation mechanism in ALD: a) ligand exchange, b) dissociation and c) association.

Chemical composition of ALD thin films

ALD thin films usually have some impurities in chemical composition. It is affected by chosen deposition conditions.

One reason is the purity of precursors (or reactor). If the precursors contain some volatile reactive impurities, then the elements from those can later appear also in film composition. It is possible to get some impurities from the carrier gas or the deposition system itself.
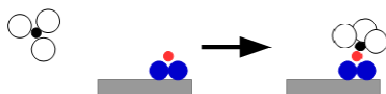
The second reason of impurities is the deposition reaction and how it is conducted. The ligand exchange during deposition on the substrate surface between precursor molecules requires infinitesimally long time to go through full conversion. The precursor pulse times are regularly shorter than suitable for that purpose. This can be somewhat regulated by choosing longer pulses, but, for practically reasonable conditions, some impurity usually has to be accepted.

Again, for instance, if the purge pulses are too short, some of the volatile material does not have enough time to desorb from the substrate, therefore leaving residual material (precursor or an element it contains, reaction products) on the surface, which could be covered by another layer of deposit and hence will stay in the film.

There is always possibility that all the reactive centers on the substrate might not give desired reaction and form required bonds. For instance, in AlCl$_3$ and

water process, inclusions of chloride and hydrogen can be expected in the composition of an ALD film.

The third way ALD film composition is affected is the selection of suitable deposition temperature. High temperatures can increase the content of impurities, especially if metal-organic (alkoxides, alkylamides *etc*.) precursors are used. The precursors could start to decompose in gas phase and uncontrollable species from precursor molecule deposit on the substrate. The species most likely would include undesired atoms, *i. e.* carbon, hydrogen. Although, hydrogen could be removed by post-deposition heat treatment, the heavier elements still remain in the deposit.

Crystallinity of ALD thin films

Depending on chosen precursors and conditions, ALD thin films can appear in several different crystallographic phases, which can be measured using, for instance, X-ray diffraction (XRD) or Raman spectroscopy [21]. The claim of amorphous or non-amorphous should be treated with some reservation. There is usually a limit, where crystals are too small (or too few) for detection with a method/device. In that case, if the measurement was done by XRD, the film rather should be called XRD amorphous. Hereinafter this idea should be reminded, when reading about amorphous crystallographic phases.

In ALD, the crystallinity of the deposit can be affected by deposition temperature. Depositing TiO_2 from $TiCl_4$ and H_2O, would give amorphous thin film below about 125 °C, at 150 °C anatase phase starts to form, and from 300 °C the rutile phase starts to contribute to the phase composition [29,30]. The same is valid for ZrO_2 and HfO_2 – in certain temperature ranges certain phases tend to preferably appear and, sometimes, dominate. At lower temperatures (200 °C) the films appear as almost amorphous and begin noticeably crystallize at deposition temperatures of 300 °C and higher. In HfO_2 the monoclinic phase usually prevails and in ZrO_2 the mixture of tetragonal and monoclinic phases is more pronounced [31].

Compared to the ionic metal oxides, *e. g.* HfO_2 and ZrO_2, the ALD of more relevant, and therefore glassy, oxides, such as Al_2O_3 results in highly dis-ordered, amorphous solid films. Deposition of Al_2O_3 from trimethylaluminum $Al(CH_3)_3$ (TMA) and water, definitely results in amorphous thin films in the substrate temperature range of 20–400 °C. At higher temperatures, TMA decomposes thermally rather intensively, and the control over deposition with atomic layer precision becomes lost. If aluminum chloride, $AlCl_3$, were used instead of TMA, the deposition temperatures could be extended to 800–900 °C, and some crystallization *in situ*, during the growth, could be considered [21].
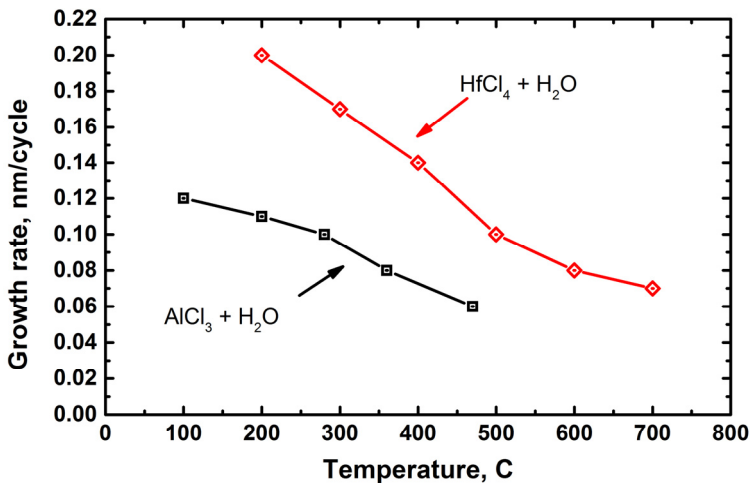
Deposition rate

It has been mentioned in previous chapters that ALD is capable of depositing materials in layer-by-layer manner. As the unit cell of a crystalline material size is well below 1 nm, the deposition rate in ALD is not very high compared to regular CVD, which can easily have rates 1 µm per hour or minute [32]. Some average growth rates for ALD oxides deposited from chlorides and water at 300 °C are shown in Table II.

Table II. Deposition rates for several single oxides deposited by atomic layer deposition.

Material	Rate, nm/cycle	Ref.
Al_2O_3	0.10 (at 280 °C)	[33]
HfO_2	0.17	[34]
Ta_2O_5	0.06	[35]
TiO_2	0.07	[36]
ZrO_2	0.13	[37]

Considering the rates shown in the Table II, the growth of a HfO_2 film to the thickness of 1 µm would take 18 hours to deposit using pulse times 2/2/2/5 seconds. Under the same reactor conditions depositing the same thickness of TiO_2 would take over 43 hours.

The total deposition time also depends on temperature. Figure 3 can be reconstructed based on data from [33] and [34]. The temperature affects the adsorption-desorption balance, reaction speed and through that the thin film growth rate, which could gradually reduce at increasing temperatures (from instance in chloride related processes).


Figure 3. Growth rate as function of deposition temperature in ALD [33,34].

ALD "window"

All the topics discussed so far can be gathered together to an ALD concept called "ALD window" (Fig. 4). A precursor can go through six stages concerning the process temperature. If the temperature is too low the precursors might condensate on a substrate and result in uncontrolled amounts of the material deposited. Alternatively, at low temperatures, there might not be enough energy at low temperatures to activate the reaction and this could result in incomplete reactions. These effects can be diminished if temperature is increased to promote desorption and energize precursor molecules. If the temperature is increased too much for the given precursor, desorption may start to limit the deposition rate – the molecules do not stay on the substrate for time needed to meet and react with the second precursor. Additionally, as discussed above, and quite commonly in the case of alkylamide and alkoxide types of precursors, the precursors can start to decompose to non-volatile compounds, at high temperatures, which could then precipitate on the substrate and increase the growth rate in poorly controllable ways.
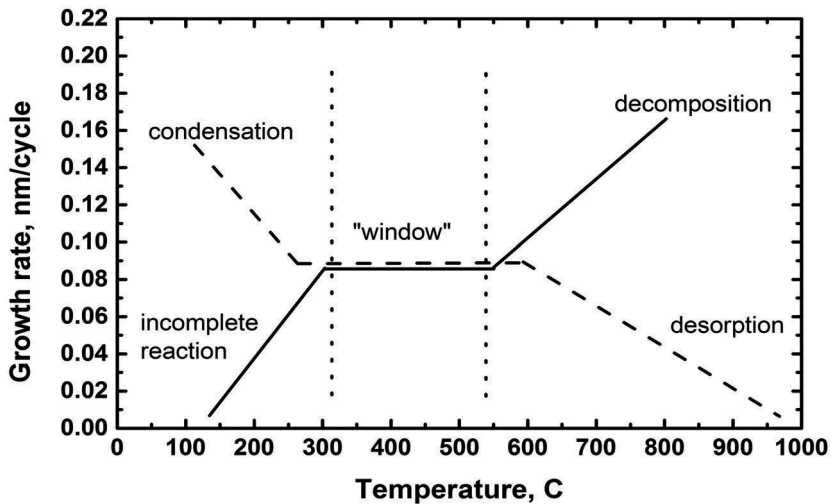
Figure 4. ALD window – a region where ALD-type, *i. e.* substrate controlled, self-limiting, and parameter dependent, thin film growth could be possible.

Deposition monitoring using quartz crystal microbalance measurement – QCM

The ALD window can be monitored in real time and, sometimes, even the ALD window can be found using quartz crystal measurement technique [38,39,30]. The method is based on using oscillating quartz crystal (or crystals), which is placed in the reactor chamber during deposition for the detection of adsorption

of monomolecular layers with masses in the order of nanograms per cycle. The crystal is opened from one or all sides to the gas flows in the chamber. When an adsorption process occurs, the resonant frequency of the crystal drops (similarly to the oscillation of a mechanical pendulum when it's mass were increased suddenly). The change is proportionally related to the total mass of molecular layer on the crystal and precursor adsorption-desorption behavior, *i. e.* exponential drop-or-rise in frequency, respectively, can be monitored.

The condensation and decomposition of a precursor would both result in exponentially increasing frequency drop, although the absolute rates are usually different, continuous in the time scale axis. Condensation and decomposition are, however, not expected or desired phenomena in any well-defined ALD process. Figure 5 shows what happens to quartz crystal frequency signal if the precursors rather condense on the crystal. The increasing height of the "saw teeth" indicates that step-by-step the residue amount on the crystal increases.
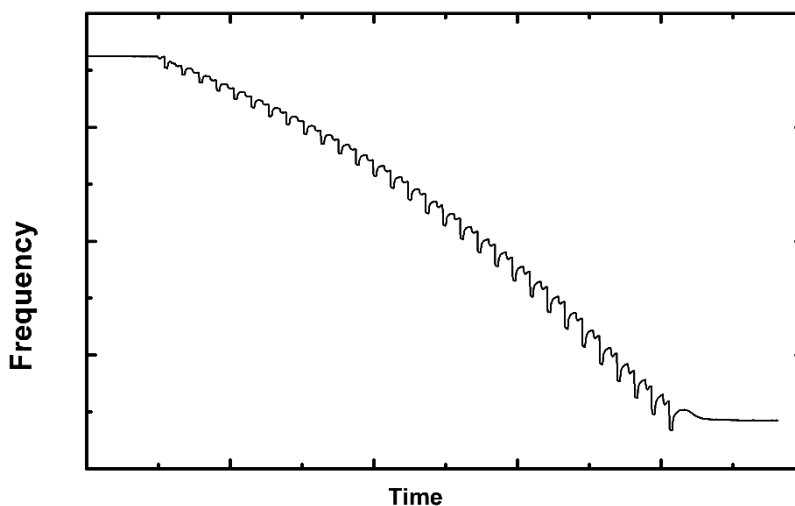
Figure 5. QCM measurements of 2 s TMA and 2 s water pulses during 30 cycles at room temperature (purges were 2 and 5 s, respectively). The increasing signal drop during each successive full cycle indicates that process is not going through pure ALD-type deposition. Most likely some material is not desorbing well due to low temperature and exponentially increases signal change.

A QCM signal during ALD using TMA and $TaCl_5$ is shown in Figure 6. The graph shows 2 cycles of deposition, starting with TMA (3 s) succeeded by the first 2 s N_2 purge pulse, 2 s $TaCl_5$ pulse and the second 5 s N_2 purge pulse. For the interest of accuracy 10–30 cycles are deposited and the frequency change calculated. Usually few cycles from the start are omitted due to the so called deposition incubation effect or nucleation phase [40], when the steady state growth is not achieved. This can appear for instance when depositing nanolaminates, where an oxide alternates with another or when depositing oxide

mixtures. It is the result of steric hindrance which prevents molecules to reach suitable active surface species.
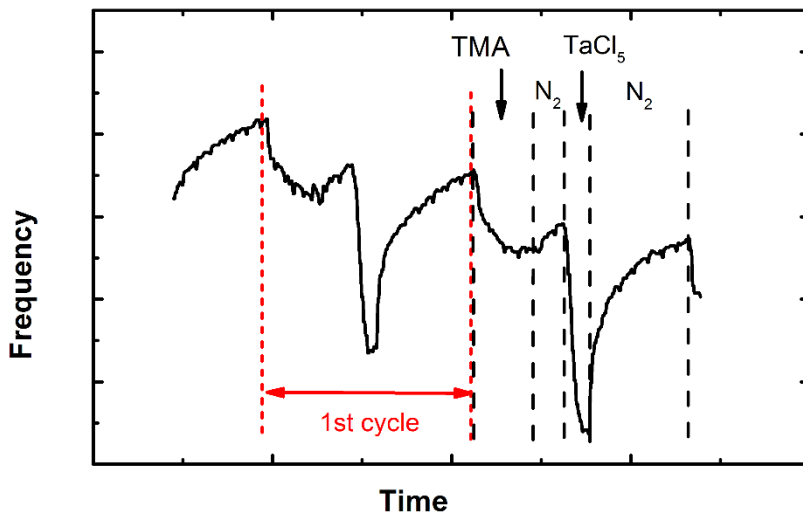
Figure 6. A quartz crystal signal during 2 cycles of ALD-type carbon deposition process. Notice the resemblance to exponential change in line during TMA pulse and second nitrogen purge pulse, but not really seen during the other pulses.

The application of the QCM method involves certain complications. The oscillation frequency of the crystal is very sensitive to temperature changes, often expressed as corresponding drift in the baseline frequency, if the reactor temperature is not perfectly stabilized. The reactor temperature together with its effect to the QCM vibration frequency can, under our reactor conditions, be stabilized to deviations within ±0.5 Hz/min, but during the drift within the whole deposition process the change would still measure in hundreds of hertz's. This means, in practice, that the operator has to wait until the thermal equilibrium is truly achieved and then start the measurements. The mechanical vibrations and bad electrical contacts can also give some additional noise to the signal reading, though.
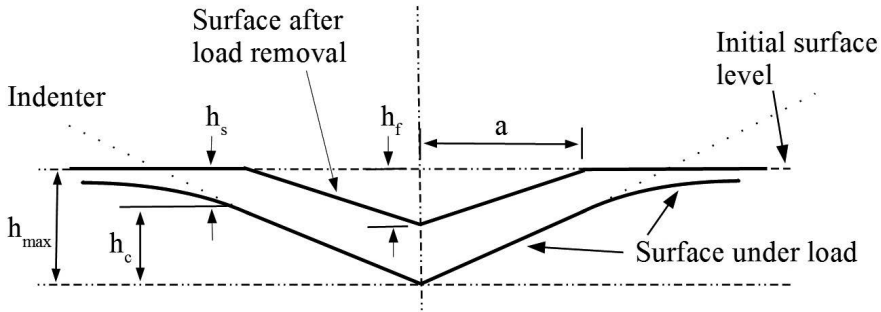
NANOINDENTATION

Hardness can be described as a material resistance to plastic deformation. In macroscopic level, most likely the oldest and most used hardness measurement scales are those of Brinell and Rockwell. In addition, Knoop and Vickers scales are used quite often [41]. The indentation depth after Brinell and Rockwell are in the range of millimeter or tenth of that and for Knoop and Vickers indentations, the depths are in the range of several to tens of micrometers.

The interest, both academic and industrial, of thin functional films on a bulk substrate demanded for new measurement techniques to characterize mechanics of the films, which were in thicknesses of few microns or even thinner. Therefore, nanoindentation techniques were developed for the characterization of thin films, were the indenter (also called Berkovich indenter) tip displacements could be as low as few tens of nanometers [10].

The theoretical basis for nanoindentation techniques were presented by Doerner and Nix in 1986 and further developed by Oliver and Pharr in 1992, which is the standard approach nowadays [42,43,11,12]. The analysis of Oliver and Pharr was based on mathematical models for different indenter geometries, first analyzed by Sneddon in 1965 [44]. Their starting point was the experimentally proven process taking place during indentation (Fig. 7).

An equally 3-sided (diamond) pyramid, Berkovich indenter, with a 65.3° face to center line angle is displaced into a sample, reaching a total depth of h_{max}. As the loading is stopped, the material will partly recover due to elasticity and after removal of the tip, an indent with final depth h_f is left in the sample. The value of h_s reflects the displacement of the surface perimeter after the indentation.

Figure 7. Graphical description of processes and properties during instrumented nanoindentation [11].

Parameter a is used to calculate the projected area.

Oliver and Pharr indicated that the reduced modulus E_r can be calculated as:

$$E_r = \frac{\sqrt{\pi}}{2} \frac{S}{\sqrt{A}},$$ Equation 2

where S is contact stiffness and A is the contact area at maximum P, *i.e.* P_{max} (Fig. 8). The hardness H can be calculated as:

$$H = \frac{P_{max}}{A} \qquad \text{Equation 3}$$

S can be calculated at P_{max} from indentation data and A can be determined through calibration using a reference material with known properties (fused quartz, for instance), because the results for E_r should be the same for every indentation depth (contact area).
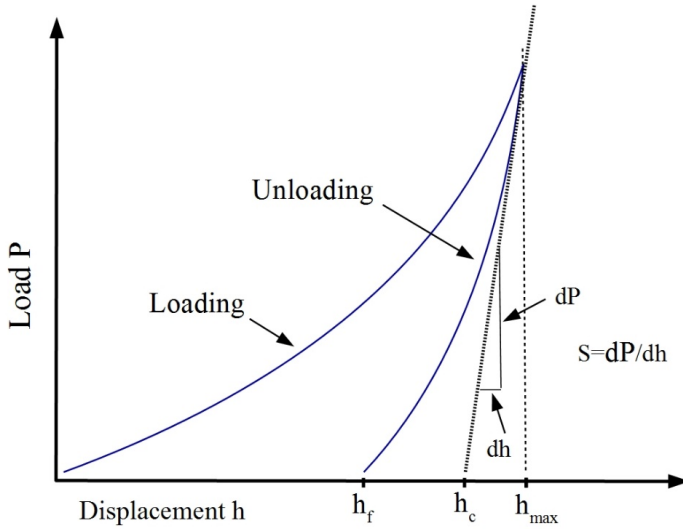
Figure 8. A load-unload graph of a nanoindentation [11].

It has been found that, for perfect Berkovich indenter, A is function of h_c:

$$A = F(h_c) = 24.5h_c^2 \qquad \text{Equation 4}$$

The meaning of reduced modulus is in the assumption that additionally to the material under investigation, the indenter material itself will deform also. To take this effect into account, the following equation can be used:

$$\frac{1}{E_r} = \frac{1-\nu_i^2}{E_i} + \frac{1-\nu^2}{E} , \qquad \text{Equation 5}$$

where E_i and ν_i are the modulus and Poisson coefficient, respectively, of the indenter material (for diamond $E=1140\ GPa$ and $\nu_i =0.07$), and E and ν are the same parameters for the specimen.

Another specific instrumented nanoindentation method for measuring mechanical properties is continuous stiffness measurement (CSM) [45,46]. It

differs from regular nanoindentation in a way that the unloading part of the nanoindentation is actually not necessary. This is achieved by using oscillating loading of the sample during stiffness S measurement. If the driving force P is expressed as:

$$P = P_{os}exp(i\omega t)$$ Equation 6

P_{os} is the applied load during an oscillation. The displacement response, $h(\omega)$, is written as follows:

$$h(\omega) = h_0 exp(i\omega t + \varphi)$$ Equation 7

(h_0 is displacement during an oscillation) then:

$$\left|\frac{P_{os}}{h(\omega)}\right| = \sqrt{\left\{\left(\frac{1}{S} + \frac{1}{K_f}\right) + K_s - m\omega^2\right\}^2 + \omega^2 C^2} ,$$ Equation 8

where S is contact stiffness, K_f is the stiffness of the indenter frame, K_s is the spring constant of the indenter system, m is the mass of the indenter, ω is the oscillation frequency in radians and C is the damping coefficient due to the air between capacitor plate displacement system (Fig. 9).
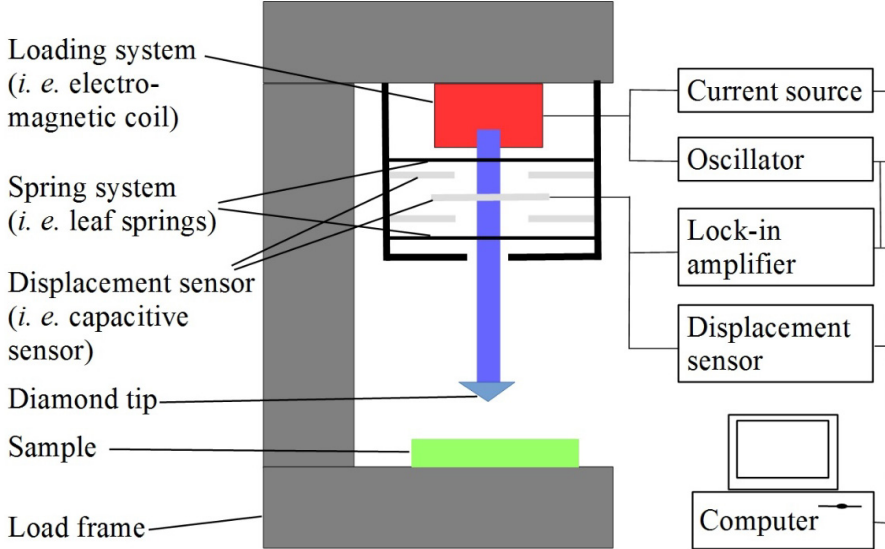
Figure 9. A schematic of an indenter system.

The oscillation force and amplitude are usually few orders of magnitude smaller than the total exerted force and amplitude. The exact values are matter of technical solutions and expertise of device developers, but possible values have been up to few millinewtons for force and few nanometers in amplitude. The oscillation frequency is usually a variable in a wide range from fractions of a hertz up to few kilohertz.

The continuous stiffness method is considered to be somewhat more precise than that determining the modulus from single load-unload curve, because the evaluation of modulus is done several times per second (for every oscillation cycle) and there are no uncertainties related to the stiffness determination during the total unloading [12,42]. Still an uncertainty caused by indenter tip area has to be considered and, empirically, it has been concluded that the data below 50 nm of displacement are not really trustworthy

Another situation where using CSM is beneficial, due to possibility to measure properties step-by-step from outside to inside, is characterizing materials with gradient modulus (modulus/hardness changes from sample surface to inward). For a homogeneous material the stiffness is linearly correlated to the displacement, but for a material with softer internal regions the stiffness will reduce, whereas for a material stiffer in its bulk, the S will increase (Fig. 10).
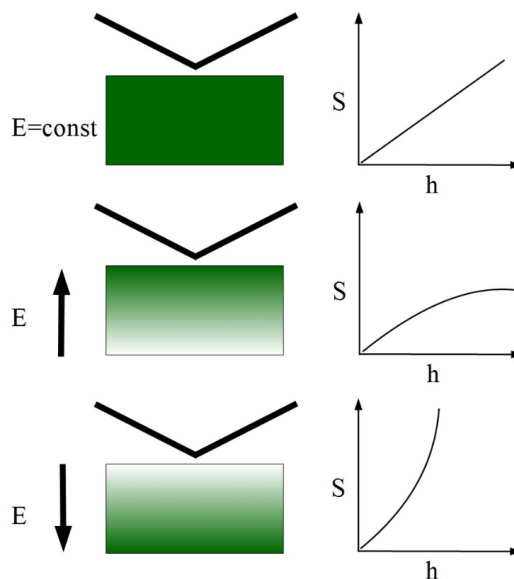
Figure 10. Correlation between contact stiffness, displacement depth and modulus. If the material is homogeneous, then S and h are linearly correlated, otherwise the stiffness will decrease with h (*i. e.* material is stiffer on outside) or increase (*i. e.* the material is harder inside) [45].

This basically allows to profile the change of material properties and is especially useful, for instance, for analyzing alloys with hardened cases or thin films on a substrate [45].

MECHANICAL PROPERTIES OF COMPOSITES

In this thesis the properties of ALD thin films on glass substrates will be calculated as mechanical properties of a composite, where one component is the glass and the other is the thin film. Prior to the calculations some theoretical background should be introduced as follows.

There are several ways to calculate and model mechanics of composite materials and some comprehensive treatments on the topic can be found in literature [13,47].

The rule of mixtures in general

The simplest models can be developed by considering a material or layers of materials as springs. This constitutes that if the layers are on top of each other and the forces are applied transversely, every layer is represented as a spring forming an array of parallel connected springs. Another bounding requirement is that the "springs" are subjected to the same strain (isostatic strain), which happens when all components are loaded at the same time [13 pg. 409]. This leads to simple linear relationship:

$$P = \sum_{i=1}^{n} v_i P_i \; , \hspace{3cm} \text{Equation 9}$$

where P is a bulk property, P_i is the property of i-th component and v_i is the volume fraction of the i-th component:

$$v_i = V_i / V \; , \hspace{3cm} \text{Equation 10}$$

where V_i is the volume of the i-th component and V is the total volume of the material under investigation. It has to be pointed out that:

$$\sum_{i=1}^{n} v_i = 1 \hspace{3cm} \text{Equation 11}$$

For a two component filler-matrix system the Eq. 9 reduces to:

$$P = v_f P_f + v_m P_m \; , \hspace{3cm} \text{Equation 12}$$

where f designates the respective property of the filler (fibers for instance) and m designates the property of the matrix material. All the rules of mixtures consider that $P_f > P_m$. It can be deduced from Eq. 4 that the properties of a composite will resemble to the filler in case of $v_m = 0$ and vice versa. Equation 12 has some use if the applied force is parallel to the fibers, for instance in a glass fiber polymer composite.

Using the analogy to springs (in series alignment in this case) a transverse response (transverse to fibers/layers) can be expressed as a reciprocal relationship:

$$\frac{1}{P} = \sum_{i=1}^{n} \frac{v_i}{P_i}, \qquad \text{Equation 13}$$

In Eq. 13 it is assumed that the stress is equally divided (isostatic stress) to each component.

Again, for a two-component system the Eq. 13 can be written as:

$$\frac{1}{P} = \frac{v_f}{P_f} + \frac{v_m}{P_m}, \qquad \text{Equation 14}$$

Equation 9 and Equation 13 are known as the rule of mixtures. The first equation for calculating material effective properties was published by Voigt in 1889 and the second one by Reuss in 1929 [48,49]. These equations define the upper bound (Voigt bound) and lower bound (Reuss bound) where the properties of a composite structure should be as calculated for a certain filler and matrix volume mixtures (Fig. 11).
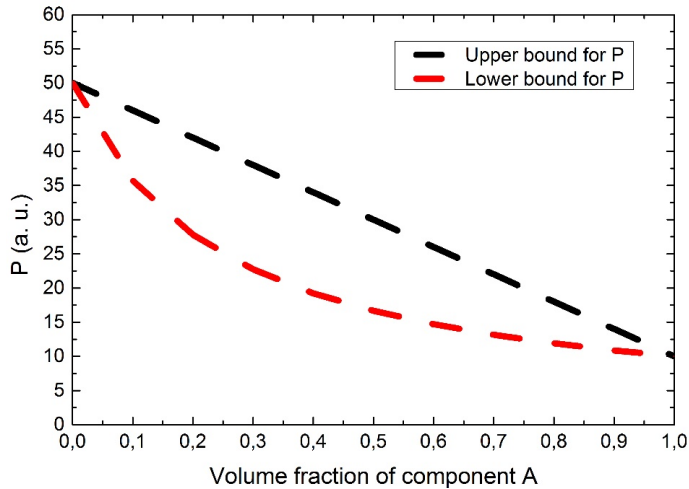
Figure 11. Representation of upper and lower bounds according to Voigt and Reuss equations. Component A has P=10 a. u. and component B has P=50 a. u.

In the laminates a property could be characterized by upper bound if the force is applied parallel to the layers (direction 1) and lower bound in case of transverse direction (in plane of directions 2–3) (Fig. 12). It should be noted that for symmetrical laminated system, the directions 1 and 2 coincide. If the layers are distributed evenly throughout the whole composite, the volume fractions of components in Voigt bound can be replaced with area fractions of the components derived from the corresponding (transverse to force) cross-section of the composite sample.
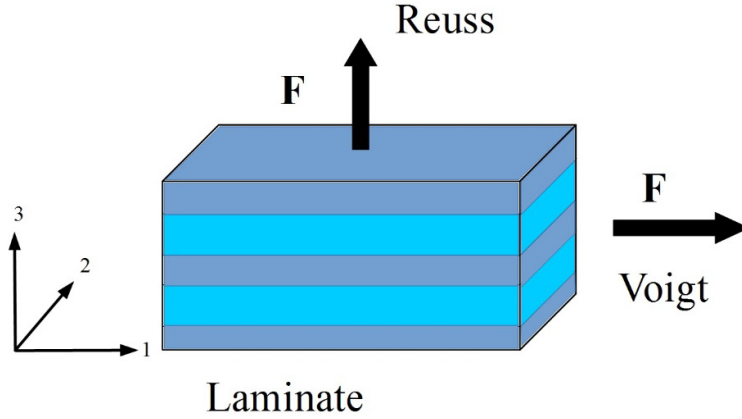
Figure 12. Simplistic representation of when to use Voigt or Reuss bounds in case of a laminated structure. A 3-axis orientation is shown also.

Derivation of rules of mixtures for modulus of elasticity

The derivation of rule of mixtures can be started using general Hooke's law between the elements of stress $\boldsymbol{\sigma}$ and strain $\boldsymbol{\varepsilon}$ tensors:

$$\boldsymbol{\sigma} = \boldsymbol{C}\boldsymbol{\varepsilon}$$
<div align="right">Equation 15</div>

The constant $\boldsymbol{C}$ is called a stiffness constant which is taken here as modulus of elasticity $\boldsymbol{E}$, therefore Eq. 15 takes form:

$$\boldsymbol{\sigma} = \boldsymbol{E}\boldsymbol{\varepsilon}$$
<div align="right">Equation 16</div>

In case of isostatic strain, all material components have to have the same strain and every component can contribute to the stress equally to its volume part, therefore:

$$\sigma = E\varepsilon = \sum_{i=1}^{n} E_i \, \varepsilon_i = \sum_{i=1}^{n} \sigma_i \, v_i \, ,$$
<div align="right">Equation 17</div>

where i designates i-th component, v_i and σ_i are respectively the volume part and stress of the i-th component. As stated before, the strains are all equal and taking into account Eq. 16, where dividing with ε will give the result as E, the Eq. 17 transforms for moduli to:

$$E = \sum_{i=1}^{n} E_i \, v_i$$
<div align="right">Equation 18</div>

For a two-component material Eq. 18 can be rewritten as:

$$E = E_1 v_1 + E_2 v_2$$
<div align="right">Equation 19</div>

or taking into account Eq. 11:

$$Ev = E_1 v_1 + E_2 v_2 \qquad \text{Equation 20}$$

This is identical to Eq. 12, where properties indexed as 1 and 2 are designated as filler (reinforcing fibers, particles *etc.*) and matrix (a clue, metal or other compliant material), respectively.

The same derivation can be done while isostatic stress is assumed. In this case all material components have to have the same stress and every component can contribute to the strain equally to its volume part, therefore:

$$\varepsilon = \frac{\sigma}{E} = \sum_{i=1}^{n} \frac{\sigma_i}{E_i} = \sum_{i=1}^{n} \frac{\sigma_i}{E_i} v_i \ , \qquad \text{Equation 21}$$

where i designates i-th component, v_i and σ_i are respectively the volume part and stress of the i-th component. As stated before, the stresses are all equal and taking into account Eq. 16, where dividing with σ will give the result as E, the Eq. 17 transforms for moduli to:

$$\frac{1}{E} = \sum_{i=1}^{n} \frac{1}{E_i} v_i \qquad \text{Equation 22}$$

For a two-component material Eq. 22 can be rewritten as:

$$\frac{1}{E} = v_1 \frac{1}{E_1} + v_2 \frac{1}{E_2} = \frac{v_1}{E_1} + \frac{v_2}{E_2} \qquad \text{Equation 23}$$

or taking into account Eq. 11:

$$\frac{v}{E} = \frac{v_1}{E_1} + \frac{v_2}{E_2} \qquad \text{Equation 24}$$

This is identical to Eq. 14, where properties indexed as 1 and 2 are designated as filler (reinforcing fibers, particles *etc.*) and matrix (a clue, metal or other compliant material), respectively. The inverse values of moduli are used here and subsequently sometimes Eq. 23 is called inverse rule of mixture.

Although the rules of mixtures are simple, these are not really applicable or find limited use, because the bounds cover wide area and most properties of composites fall between narrower limits. The Voigt bound has tendency to overestimate and the inverse rule of mixture usually tends to underestimate the properties. Both theories have premises (constant stress or strain in all components), which are not usually true (materials have different Poisson coefficients creating different stresses/strains) in real applications. Therefore, it is important to find tighter bounds.

The Halpin-Tsai relationship

The Halpin-Tsai relationship is a semi-empirical model developed and published by Halpin, Tsai and Ashton in 1969 [50–52, 13 pg. 421]. It is widely applicable relatively simple equation for two-component systems:

$$P = P_m \left(\frac{1+\xi\chi v_f}{1-\chi v_f} \right)$$

Equation 25

Here χ is:

$$\chi = \frac{P_f - P_m}{P_f + \xi P_m}$$

Equation 26

P is the composite property, P_m and P_f are matrix and filler property, respectively, and v_f is the volume part of the filler. ζ is basically an arbitrary scaling parameter, which is used to mathematically fit a curve to the results of P (Fig. 13).
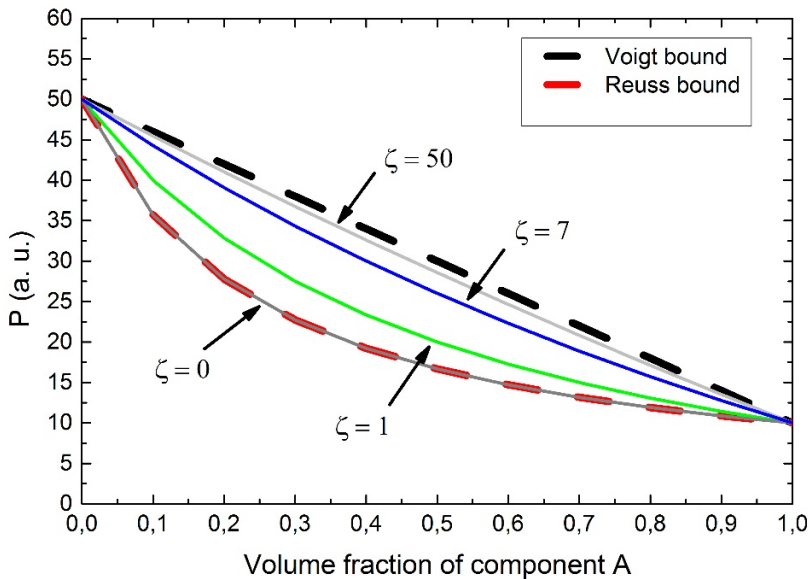
Figure 13. Halpin-Tsai model showing results for several values of ζ. As a comparison the Voigt and Reuss bounds are shown, also seen in Figure.

As it can be seen on Figure 13, the higher the value of ζ, the closer its prediction get to Voigt bound and if $\zeta=\infty$, the model coincides with Voigt; in case of $\zeta=0$, the model coincides with Reuss bound. Therefore, it can be said that the predictions with Halpin-Tsai model can be calculated anywhere in-between Voigt and Reuss bounds, which is the reason for its wide application.

The ζ can be obtained from experiments, where P is substituted with experimental value P_{ex} measured for a known specific volume fractions of components and Eq. 25 is solved for unknown ζ to give:

$$\xi = \frac{P_f(P_{ex}-P_m)-v_f P_{ex}(P_f-P_m)}{P_m[(P_f-P_m)-(1-v_f)(P_f-P_m)]}$$
Equation 27

Once the ζ has been determined for one mixture of materials, the property P can be predicted for any other mixture.

It is recognized that ζ depends on the fiber cross-section (transverse) aspect ratio a/b (a and b are lengths of the sides of a fiber with a rectangular cross-section) and how the fibers are packed (*i.e.* a square or hexagonal array). It has been shown that effective shear modulus can be fit with $\zeta=(\sqrt{3})\ln(a/b)$ and transverse Young's modulus was fit by $\zeta=2(a/b)$ for a composite with hexagonally packed fibers [53]. For circular fibers in hexagonal array, a $\zeta=1$ gives relatively good results and a $\zeta=2$ can be used as fit for square packing [13 pg. 422].

Lewis-Nielsen relationship

The Halpin-Tsai relationship is best suited for composites with fiber or plate-like reinforcement. But in case of particle reinforcement, it tends to underestimate Young's modulus for particle volume fraction $v_f>0.4$. Another drawback is that it does not account the fact that the fibers or particles can be used only up to certain amount. This comes from the possible packing density of fibers/particles. For example, if the spherical particles are considered to take position in cube corners (similarly to cubic crystal phase), the packing density can be no more than $v_f^{max}=0.52$, for body centered packing $v_f^{max}=0.60$ and for hexagonal or face centered packing $v_f^{max}=0.74$. In "random" packing the v_f^{max} is taken as the equal mixture of all previous values, resulting in a $v_f^{max}\approx 2/3$. This is taken into account in Lewis-Nielsen relationship proposed in 1970, which is given for lower bound as [54]:

$$P = \frac{1+\xi_l \chi v_f}{1-\chi v_a v_f},$$
Equation 28

where ζ_l is arbitrary fitting parameter for lower bound, v_f is volume fraction of particles; v_a is average volume fraction calculated as:

$$v_a = 1 + \left[\frac{\left(1-v_f^{max}\right)}{\left(v_f^{max}\right)^2}\right]$$
Equation 29

Here χ is calculated as:

$$\chi = \frac{P_f - P_m}{P_0 + \xi_l P_m},$$

Equation 30

where P_0 is the property as calculated according to Reuss model ($\zeta=0$).

Lewis and Nielsen considered as P only material bulk modulus K or shear modulus G. After those are found, E and v can be calculated in accord with formulas:

$$E = \frac{9KG}{3K+G}$$

Equation 31

$$v = \frac{3K-2G}{2(3K+G)}$$

Equation 32

S-mixing rule

It has turned out that Lewis-Nielsen relationship overestimates the composite properties at high particle concentrations. To encounter this, McGee and McCullough included a proportionality factor ψ into the Lewis-Nielsen model [55]:

$$P = P_m \left(\frac{1 + \xi_l \chi v_f}{1 - \psi \chi v_f} \right)$$

Equation 33

with

$$\chi = \frac{P_f - P_m}{P_f + \xi_l P_m}$$

Equation 34

In case of $P_f \gg P_m$ and $v_f \zeta_u \gg 1$, the correction factor reduces to:

$$\psi \cong 1 + \left(\frac{v_m}{\phi_c} \right) - [v_f \phi_c + v_m (1 - \phi_c]$$

Equation 35

φ_c designates a critical volume fraction, where in case of $v_f = \varphi_c$ the model behavior tends towards upper bound and in case of $v_m = \varphi_c$ the behavior tends to lower bound.

If the critical volume fraction is given the value of "randomly" packed particles $\varphi_c \approx 2/3$ then:

$$\psi \approx 1 + \frac{1}{2} \left(1 - v_f^2 \right)$$

Equation 36

For comparison, the v_a in Lewis-Nielsen model can be calculated as:

$$v_a = 1 + \frac{3}{4}v_f \qquad \text{Equation 37}$$

As a final note, it is again reminded that Lewis-Nielsen and its improved version, S-mixture model, consider the property *P* as bulk modulus *K* or shear modulus *G*. Equation 31 and Equation 32 could be used to calculate Young's modulus and Poisson coefficient.

Isotropic properties of planar alternating lamina systems

In this chapter the derivation presented in [47 pg. 137] is shown. The materials are considered to be homogeneous isotropic linearly elastic materials. Geometrically the structure consists two laminae of two different materials. One has thickness of h_1 and the other h_2 and the corresponding isotropic properties of E_1 h_1 and E_2 h_2. The laminae are considered to be infinitely large so no edge effects could appear and are neglected.

To a state of plane stress, the two-dimensional conditions of interest are relevant. It suffices to consider the planar deformation of a two material combination with total thickness of $h_1+h_2=h$, with no surface tractions on the lateral surfaces. The efficient planar shear modulus can be written for parallel arrangement:

$$G = \frac{1}{h}(h_1 G_1 + h_2 G_2) \qquad \text{Equation 38}$$

For plane stress, in x-y coordinates, the general form of stress-strain relationship is:

$$\sigma_{xx} = \frac{E}{(1-v^2)}\left(\varepsilon_{xx} + v\varepsilon_{yy}\right) \qquad \text{Equation 39}$$

and

$$\sigma_{yy} = \frac{E}{(1-v^2)}\left(\varepsilon_{yy} + v\varepsilon_{xx}\right), \qquad \text{Equation 40}$$

where v is a Poisson coefficient. If $\varepsilon_{yy}=0$, the average stress over the double-layer system is:

$$\sigma_{xx} = \frac{1}{h}\left(h_1 \frac{E_1}{1-v_1^2} + h_2 \frac{E_2}{1-v_2^2}\right) \qquad \text{Equation 41}$$

The appropriate statement of the effective properties related to average stress and strain is:

$$\frac{\sigma_{xx}}{\varepsilon_{xx}} = \frac{E}{1-v^2} \qquad \text{Equation 42}$$

therefore

$$\frac{E}{1-v^2} = \frac{1}{h}\left(h_1 \frac{E_1}{1-v_1^2} + h_2 \frac{E_2}{1-v_2^2}\right) \qquad \text{Equation 43}$$

Equation 38, Eq. 43together with:

$$G = \frac{E}{2(1+v)}$$ Equation 44

are sufficient to describe in-plane isotropic effective properties. It is found that:

$$Ec = E_1 c_1 + E_2 c_2 + \frac{E_1 c_1 E_2 c_2 (v_1 - v_2)^2}{[E_1 c_1 (1-v_2^2) + E_2 c_2 (1-v_1^2)]},$$ Equation 45

where $c_1 = h_1/h$ and $c_2 = h_2/h$ and $c = c_1 + c_2 = 1$.

This is another variant of the rule of mixture, which also includes the Poisson coefficients. The volume parts v has been replaced with parts of height, which does not alter the calculation results if other linear measures are taken the same for both layers. Bearing that in mind, note that Eq. 43 is basically the same as the Voigt bound, except that it includes the Poisson coefficients v, v_1 and v_2 for composite, material *1* and material *2*, respectively.

It is reminded here again that the Eq. 45 is derived for in-plane isotropic effective properties. Transverse to plane isotropic properties have to be derived to gain an equation suitable for nanoindentation modeling, because the force is applied transversely to nanolaminate during indentation. To do that, we start with rewriting matrixes of general Hooke's law for strain:

$$\varepsilon = \frac{\sigma}{C}$$ Equation 46

and the statement of the effective properties related to stress and strain changes to (analogous to previous derivation):

$$\frac{\varepsilon_{zz}}{\sigma_{zz}} = \frac{1-v^2}{E}$$ Equation 47

It can be seen that for strain the relationship for transverse isotropic property is inverse to E, which leads to:

$$\frac{1-v^2}{E} = \frac{1}{h}\left(h_1 \frac{1-v_1^2}{E_1} + h_2 \frac{1-v_2^2}{E_2}\right)$$ Equation 48

and

$$\frac{c}{E} = \frac{c_1}{E_1} + \frac{c_2}{E_2} + \frac{\frac{c_1 c_2}{E_1 E_2}(v_1 - v_2)^2}{\left[\frac{c_1(1-v_2^2)}{E_1} + \frac{c_2(1-v_1^2)}{E_2}\right]}$$ Equation 49

If $v_1 = v_2$, the term $(v_1 - v_2)^2 = 0$ and the Eq. 45 reduces to Voigt bound and Eq. 49 reduces to Reuss bound. This again clearly states that neither Voigt or Reuss

bound take difference in Poisson coefficients into account, rather presume that the coefficients coincide in every case, which is rarely the real situation. This means, in other words, that Eq. 45 and Eq. 49 should be preferred over simple Voigt and Reuss bounds. Although, this still indicates that Voigt and Reuss bounds are quite good approximations for calculating composite properties, but for limited occasions. For instance, if the difference in Poisson coefficients is 0.05, the square would be 2.5×10^{-3}, which greatly simplifies the 3rd term in Eq. 49. As an another example the moduli could be taken, for instance, $E_1=140$ and $E_2=70$ ($c_1=c_2=0.5$, $v_1=0.25$, $v_2=0.2$) and we obtain the value for 3rd term to be 6.2×10^{-6}, which is almost 1000 times smaller than first two terms. Therefore, it is quite safe to reduce Eq. 49 down to simple Reuss bound. The same goes for Eq. 48.

Effect of porosity on composite mechanical properties

Due to flaws in production and processing, ceramics might have some residual porosity in final product. Pores can be described as gas inclusions in a material. Gases do not possess any mechanically accountable elastic properties in ceramics, therefore, pores can be seen as second material phase with modulus and hardness being 0. Considering any of the rules of mixtures, if one component has mechanical properties of 0, the responding composite property will be lower than the pure base material and decreases linearly and sharply [63]. It has been found that a good approximation to take account the porosity for calculating elastic moduli is:

$$E = E_0(1 - bP) = E_0 - E_0 bP \qquad \text{Equation 50}$$

where E_0 is the Young's modulus for a compact material, P is the volume fraction of porosity and b is an empirical fitting constant, which also somewhat takes the pore morphology into account [56]. The latter is a complex problem as pores could take very different geometrical shapes hindering the development of unified theory for modeling effects of porosity.

Summary of theoretical introduction

In previous chapters an overview of basic features related to atomic layer deposition, instrumented nanoindentation and mechanical characterization are given. In the last part, several theoretical approaches with different complexities are described, which should allow to predict composite mechanical behavior and could be used to optimize the properties in practical applications. Some of the theories were tried on CSM results published in III.

EXPERIMENTAL

This chapter gives brief overview of the results found in I–IV and it is recommended to refer to articles I–IV for more complete information.

Nanocomposite of atomic layer deposited aluminum oxide on γ-alumina nanofibers

Γ-alumina nanofiber (Fig. 14) slices were coated with amorphous alumina using trimethylaluminum and water process [I]. The deposition temperatures were 150 °C and 300 °C, the amount of deposition cycles was 100.

Figure 14. Alumina nanofibers in as received form. The diameter of the fibers was 10–40 nm.

Two sets of pulse timings were used: 2/2/2/5 s and 10/10/10/30 s (corresponding to $TMA/N_2/H_2O/N_2$ pulses, respectively). Planar silicon pieces with (100) orientation were used as reference to determine the deposited film thickness. The coated fibers were heated at 1000 °C for 20 min and subjected to compaction using about 700 MPa pressure to produce compact pieces of alumina nanofiber reinforced alumina matrix composite.

Characterization was done by scanning electron microscopy, spectroscopic ellipsometry, synchrotron radiation, X-ray diffraction and Vickers hardness tester.

Atomic layer deposited aluminum oxide and silicon carbide nanoparticle composite

Silicon carbide nanopowder with average particle size of 30–40 nm was used, as reinforcement material, to make tablets, 11 mm in diameter and 50–250 µm in thickness [II]. The particles were compacted in a die with 170 MPa pressure forming a porous substrate. Trimethylaluminum and water based ALD process was used to deposit amorphous alumina matrix in the pores of SiC substrate. The deposition temperature was held at 300 ± 6 °C and the pressure was around 250 Pa. The pulse times and cycle counts are shown in Table III.

Table III. Pulse lengths and cycle counts during experimenting with SiC nanopowder tablets.

Sample No.	Pulse times, s	Cycle count
1	2/2/2/5	100
2	2/2/2/5	350
3	2/2/2/5	750
4	2/2/2/5	1000
5	5/5/5/10	100
6	10/10/10/30	100

Scanning electron microscopy, µ-Raman spectroscopy, X-ray diffraction, atomic force microscopy, spectroscopic ellipsometry and instrumented nano-indentation techniques were used to describe the aspects of experimentation. Focused ion beam was used to cut and reveal composite layer, its inner structure, on sides of the substrates.

Atomic layer deposited Al_2O_3, HfO_2, ZrO_2 and Ta_2O_5 nanolaminate composites

Four oxides and three composite systems were deposited: Ta_2O_5-Al_2O_3, Ta_2O_5-HfO_2 and Ta_2O_5-ZrO_2 [III]. The precursors were chlorides of Ta, Hf and Zr, and trimethylaluminum (TMA) for Al. Water was used as oxidizer. The deposition temperature was 300 °C and soda-lime glass (SLG) was used as the substrate. The laminates were deposited starting with an under layer of one oxide and several alternating layers of two oxides as designated in the beginning. The first layer was 10 nm in thickness (if not noted otherwise) and the alternating layers of two oxides had combined thickness of 20 nm. For example: first layer was 10 nm of Ta_2O_5 and on top of it 8 times alternating layers of 15 nm of HfO_2 and 5 nm of Ta_2O_5 or shortly 10 nm Ta_2O_5 + 8× (15 nm HfO_2 +5 nm Ta_2O_5). The total coating thicknesses were around 170 nm. The cycle count in every layer was determined by the average deposition speed (in nm/cycle) of the deposition of

pure oxides. Any hindrance or enhancement effects of growth speed during switching from deposition of one oxide to another were not taken into account.

The films were characterized with X-ray reflection (XRR) and (grazing incidence) diffraction (GIXRD), scanning electron microscopy (SEM) with focused ion beam (FIB) and instrumented nanoindentation using continuous stiffness method.

Atomic layer deposited alumina on modified steel

Aluminum oxide was deposited from trimethylaluminum and water on steel substrates (supplied by Sandvik AB, Sweden) at 300 °C [IV]. Two sets of substrates were obtained – bare steel and with 200 nm SiO_2 coating. The deposited alumina thicknesses were 18, 45 and 90 nm on both substrate types.

The samples were characterized with X-ray reflection (XRR) and (grazing incidence) diffraction (GIXRD), scanning electron microscopy (SEM), time-of-flight elastic recoil analysis (ToF-ERDA) and instrumented nanoindentation using continuous stiffness method.

RESULTS AND DISCUSSION

Nanocomposite of atomic layer deposited aluminum oxide on γ-alumina nanofibers

The structure of fibers corresponded to alumina γ-phase and the coating did not reveal any traces of crystallographic ordering, thus remaining amorphous. The results obtained by XRD and XAS measurements were consistent in this regard. SEM investigation revealed that the fiber thickness after coating might exceed expected thickness. The expectations were based on previously known growth rate (about 0.10 nm/cycle) measurements in similar conditions with the same precursors and published results [57,58]. The SEM measured fiber thickness after the deposition was about 20 nm in excess, giving a growth rate about 0.15 nm/cycle. The ellipsometry, carried out on reference alumina films on planar Si substrates, showed average growth rate to be 0.17 nm/cycle, which was in good correlation with 0.15 nm/cycle. The possible reason for the increased growth rate was that the precursors tended to adsorb conformally around the fiber bundles, at least partially (specific surface area of the fibers was around 150 m^2/g), and the purging pulses may have been too short to remove all the excess precursor molecules from the porous material. Thus, the precursors could partially mix and react also in the gas phase, and cause certain contribution from fast CVD-like process. This has led to the conclusion that special care has to be taken and more preparation might be needed when dealing with substrates with high specific area.

The surface of fiber bundles could be completely coated with dense alumina around it, depending on the pulse times chosen. The distance between fibers before the coating process was about 60–70 nm. Considering the growth rate, it could take some 400 cycles to totally seal the gaps. Although in this work such high amount of cycles was not used, some regions with narrower gaps showed fibers "clued" together after the deposition (Fig. 15).

The work also led to another conclusion – choosing the right pulse times may allow one to create a material, which has dense shell around a still porous core after deposition (Fig. 16). This could open up some interesting possibilities. For instance, it can be utilized to make fibers coated thoroughly with catalytic material and sealing the outer layer of the fiber bundle, creating a tube with catalytic nanofibers in it.
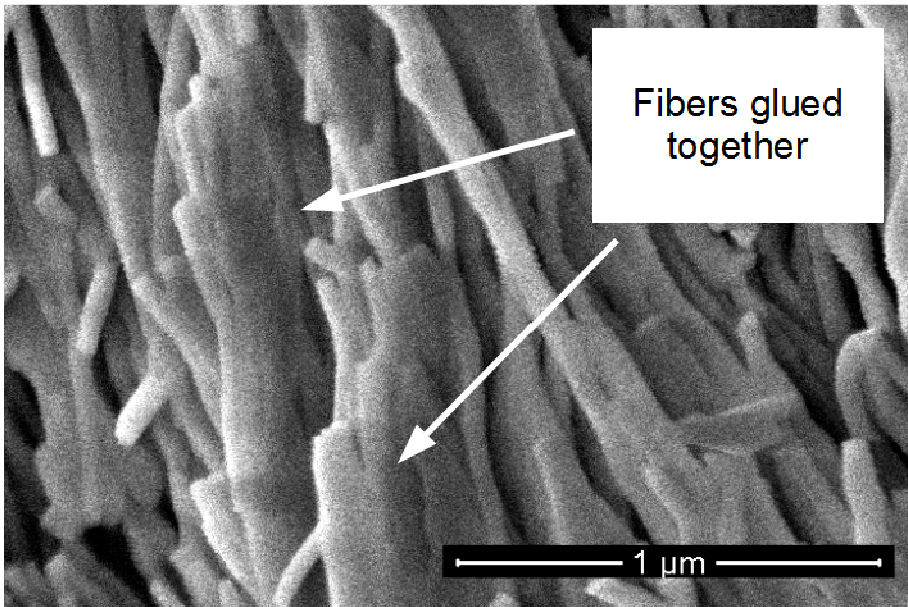
Figure 15. Alumina fibers with some parts "glued" together.
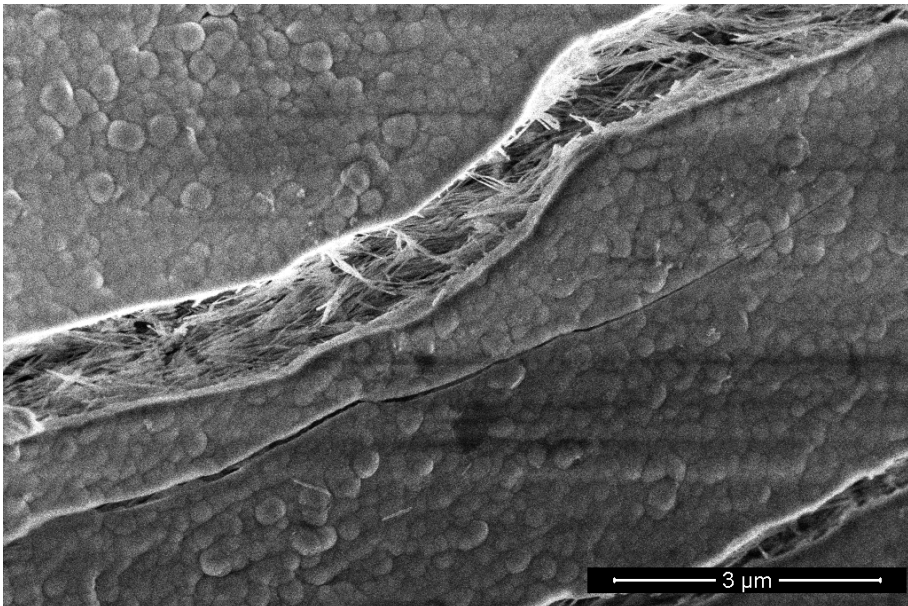
Figure 16. A surface of a sample with dense shell. The fibers can be seen in cracks and these appeared to be below the shell. The reason for cracking is unknown; one could be handling of the samples.

Compaction of the fibers with a hydraulic press was done using pure fibers, coated at 300 °C (pulse times 10/10/10/30 s) and at 150 °C (pulse times 2/2/2/5 s), Table IV. The aim was to densify nanofiber reinforced composite and then measure mechanical properties. The hardness test results obtained from the compacted fibers are presented in Table IV.

Table IV. Vickers hardness test results (100 g, standard conditions) for compacted pure fibers and coated fibers.

Sample and conditions	Hardness $HV_{0.1}$
Pure fibers	52
Fibers coated at 300 °C, 10/10/10/30 s	80.5
Fibers coated at 150 °C, 2/2/2/5 s	96

It can be seen from Table IV that the coating of the fibers had some positive effect on hardness, but the results are not comparable to hardness of fully dense alumina, which might have hardness in the range of few thousands, depending on phases and microstructure. It was noticed that microscopic cracks appeared in the compacted material, which most likely affected the results. It could be that the heating temperature prior the compaction was not high enough, resulting in weak structure and low hardness. Another reason could be that there was some thermal shock involved during cooling of the samples creating stresses in the material which resulted in poor structure.

Besides the Vickers test, no other measurements were conducted regarding the mechanical properties. It was recognized that simpler sample preparation would be beneficial, because every step in process most likely would contribute to errors, sophisticate the analysis *etc*. However, the work proved that there could be very interesting outcomes involving ALD treatment of three dimensional structures.

## Atomic layer deposited aluminum oxide and silicon carbide nanoparticle composite

The phase compositions of α-SiC and Al_2O_3 were verified before and after ALD. There was no change in the XRD patterns taken before and after ALD, revealing that the about 100 nm thick alumina was amorphous, as expected. In μ-Raman spectra, some very low intensity peaks apparent in initial α–SiC were lost in the samples after coating with alumina, but otherwise the graphs coincided. Both methods confirmed that no significant phase changes occurred during the ALD process. This could be expected as the temperature was only 300 °C.

The melting point of dense SiC is 2730 °C. For sintering, the temperature can be lower, usually down to 65–75% of the melting point can be used. The melting point for nanoparticles has been reported to be even lower than that, but

still markedly higher than 300 °C [59]. SiC is stable at such low temperatures, therefore, no phase changes could occur during ALD. This also means that no sintering effects could be involved, which could affect mechanical properties of the produced samples, therefore, any effects are derived only from deposited alumina and its interaction with SiC nanoparticles.

The film thicknesses on silicon reference substrates showed a very good correlation between cycle count and measured thickness, indicating the average growth rate to be 0.09 nm/cycle.

The surface roughness measurements with AFM showed that at least an area of 20×20 μm is good to get average estimation (Fig. 17).
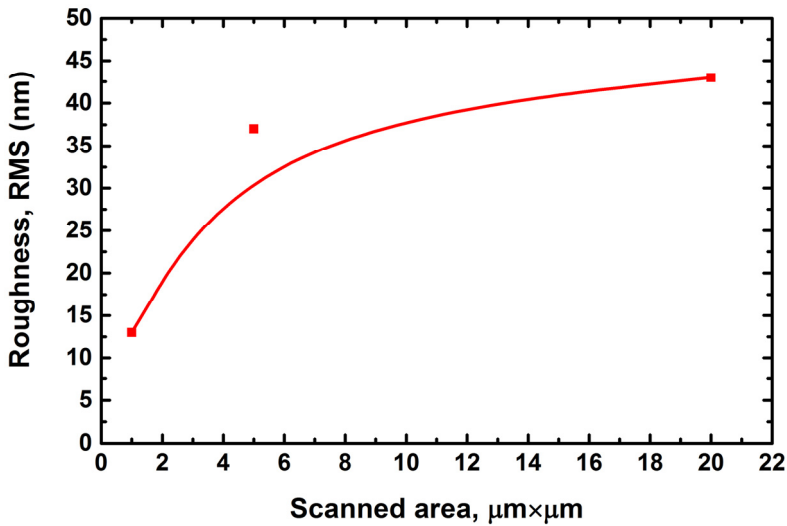
Figure 17. The quadratic mean roughness of a SiC-Al$_2$O$_3$ nanocomposite surface according to AFM measurements.

The roughness has almost levelled at around 45 nm in scanning area of 20×20 μm, which indicates that increasing the area would not increase significantly the root mean square (RMS) roughness value. The maximum height differences found in corresponding areas also levelled out at around 800 nm (to be exact, 775 nm for 20×20 μm area). This indicated that the sample surface was mostly smooth but some really deep trenches, holes (or high ridges) could be present. As the samples were used in the instrumented nanoindentation experiments as-is, without any polishing or other surface treatments, it was expected to have high deviations of hardness and modulus values. This was later confirmed.

The instrumented nanoindentation was performed at 25, 15, 5 and 2 mN forces. The last value was found to be suitable to test all samples, resulting in indentation depths of up to 160 nm. Fused silica reference was used to calibrate the indentation tip up to 320 nm depth.

The results of the indentations are gathered in Table V. It can be seen that the standard deviations are rather large. Nevertheless, the results indicate that

the samples with shorter pulses had lower moduli and somewhat lower hardnesses. The higher cycle count (at the same pulsing times) seemed to have some enhancement effect but the results were not entirely convincing yet (samples 1–4). It could be said that the moduli and hardness's stayed on the same level. On the contrary, the longer pulse times seemed to have enhancement effect on formed composite hardness and modulus, even though the cycle count was as low as 100 cycles (samples 1, 5, 6). The hardness and moduli for pure ALD alumina would be 10–14 GPa and 140–180 GPa, respectively [60] and for pure compact SiC values of 29 GPa and 316 GPa, respectively.

Table V. The results of 20 indentations of SiC-Al_2O_3 composite. Applied force was 2 mN.

Sample No.	Pulse times, s	Average hardness (st. dev.), GPa	Average modulus (st. dev.), GPa	Cycle count
1	2/2/2/5	7.7 (2.2)	46 (7)	100
2	2/2/2/5	5.4 (1.4)	35 (8)	350
3	2/2/2/5	6.8 (1.2)	50 (12)	750
4	2/2/2/5	8.1 (4.0)	60 (16)	1000
5	5/5/5/10	9.0 (1.1)	74 (9)	100
6	10/10/10/30	12.9 (2.6)	113 (17)	100

A usable conclusion could still be drawn from the results. Long precursor and purge pulses and high cycle count would likely to be needed to produce a hard nanostructured composite using pressed SiC nanopowder and atomic layer deposited Al_2O_3.
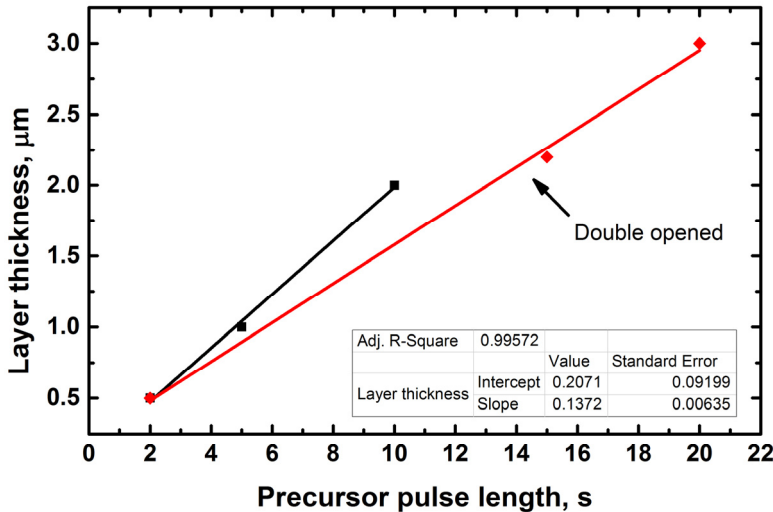

Figure 18. Difference in correlation between pulse lengths and acquired composite thickness in case the TMA dosage has been increased by opening the inlet valve 2 times.

The graphs in Figure 18 would allow one to predict the pulsing needed to produce a layer with certain thickness. For instance, to make a 5-micron thick composite it would take about 26 s pulse of lean mixture of TMA and carrying gas or 35 s TMA pulse with increased concentration (calculated from the linear equation data). This is somewhat controversial, because one would rather expect getting thicker layer in case of increased TMA flow. This might happen due to the higher concentration of precursor nearby the surface, because the purge pulses might not be long enough to purge the substrate particles. Therefore, some CVD might occur in deeper parts of the tablet and possible blockage inhibits precursor molecule movement to even deeper.

In conclusion it could be said that the work done here was a bit simpler compared to that carried out on fiber bundles (I), but still some very difficult aspect appeared. For instance, as mentioned before, the effect of residual porosity in the samples stayed unclear, leaving some open ends in the discussion. Nonetheless, it was proved that with suitable deposition conditions and materials, a SiC nanoparticle reinforced nanocomposite could be produced (see also III for additional information about ALD alumina mechanical properties).

Atomic layer deposited Al_2O_3, HfO_2, ZrO_2 and Ta_2O_5 nanolaminate composites

Most of the structural and other characterization of nanolaminates, except mechanical, was carried out earlier (refer to III). In this work the previous characterization results were partially checked and confirmed, demonstrating the stable properties of ALD thin film structures over time. The crystallinity of HfO_2 (Fig. 19) and ZrO_2 (Fig. 20) has not changed over 20 years passed since the preparation of the samples. The alumina and tantala interlayer were amorphous. The crystallinity in HfO_2 and ZrO_2 could be detected in laminate composites starting from the single interlayer thicknesses of 5 – 10 nm. The laminate structure has been retained as determined by X-ray reflection (Fig. 21).
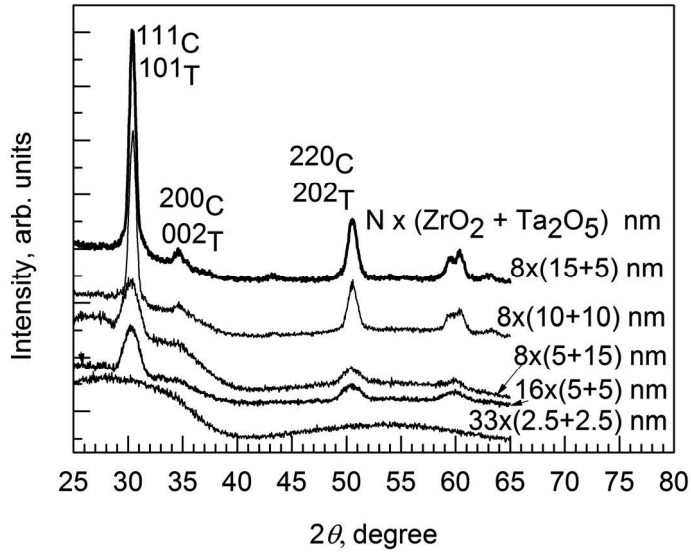
Figure 19. Grazing incidence X-ray diffraction patterns of ZrO_2-Ta_2O_5 nanolaminates. Miller indexes of the most characteristic XRD reflections are indicated. Subscripts M, T, and C, denote monoclinic, tetragonal, and cubic polymorphs, respectively. The depositions of interlayers with their nominal thicknesses are indicated as labels [61].
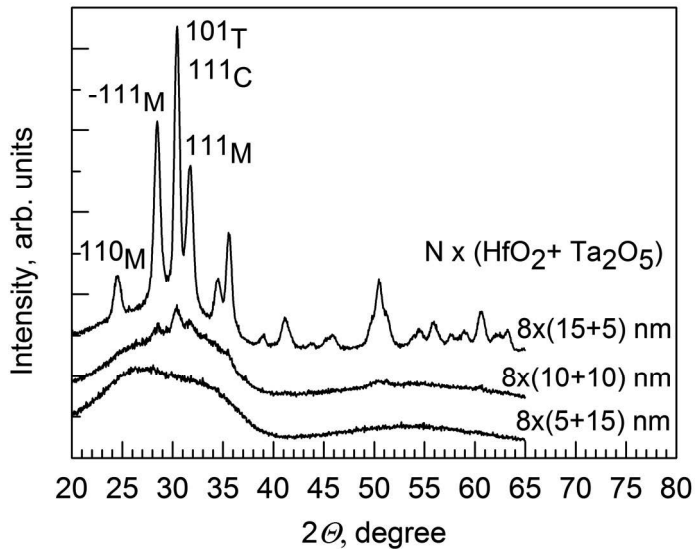

Figure 20. Grazing incidence X-ray diffraction patterns of HfO_2-Ta_2O_5 nanolaminates. Miller indexes of the most characteristic XRD reflections are indicated. Subscripts M, T, and C, denote monoclinic, tetragonal, and cubic polymorphs, respectively. The depositions of interlayers with their nominal thicknesses are indicated as labels [62].
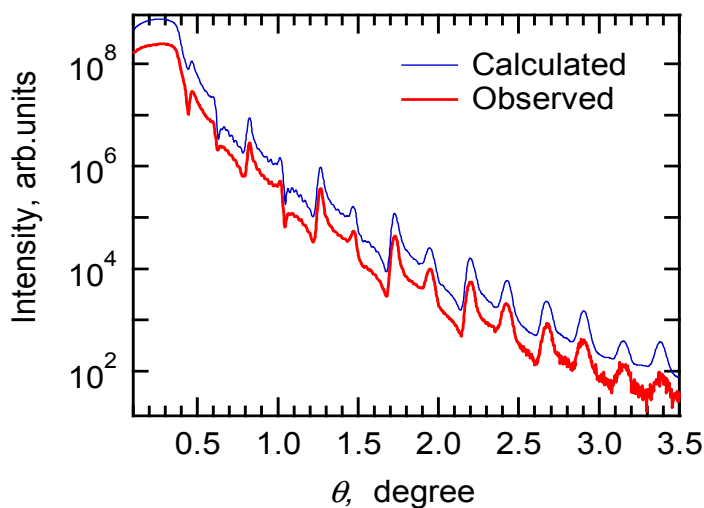
Figure 21. Representative X-ray reflection pattern from an HfO_2-Ta_2O_5 nanolaminate, obtained from a film grown with the complete sequence of constituent layers with nominal thicknesses 10 nm Ta_2O_5 + 8× (10 nm HfO_2 + 10 nm Ta_2O_5).

The laminated nanostructure was also confirmed with SEM-FIB (Fig. 22) were the alternating layers of HfO_2-Ta_2O_5 nanocomposite coting could be seen. For the sake of good quality FIB cutting a coating of platinum was also deposited beforehand. The total film thickness was around 165 nm.
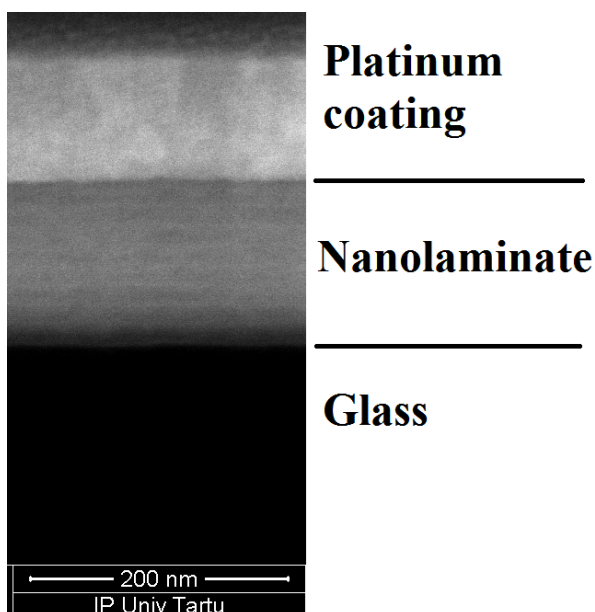
Figure 22. The microstructure of an HfO_2-Ta_2O_5 nanolaminate cut revealing alternating layers of HfO_2 and Ta_2O_5. The overall thickness of the nanolaminate was about 165 nm.

The SEM-FIB was also used to image an indentation mark in 5 nm Ta_2O_5 + 33× (2,5 nm ZrO_2 + 2,5 nm Ta_2O_5) + 5 nm Ta_2O_5 nanocomposite. Several parallel cracks on the indentation sides can be seen.

Another sample of a top view of an indentation is of 10 nm Ta_2O_5 + 8× (15 nm HfO_2 + 5 nm Ta_2O_5) nanocomposite. FIB cutting region is approximately indicated with the white line. It seems like material has been damaged intensively near indenter tip and edges. Some parallel cracks can be vaguely seen similarly to Figure 23 and Figure 24.

The focused ion beam cut can be seen on Figure 25. For a good FIB cutting a layer of conductive platinum is applied on top of the sample. From the cross-section a major crack can be seen at the left edge of the indent along with apparent delamination near it. This can be seen in more detail in Figure 26. Similar effects can be noticed at right also. In Figure 26, the structure near the indenter tip can be seen showing some voids in-between the thin film and the Pt layer. This could be due to some surface contamination before applying the Pt layer leaving residue between the thin film and platinum.
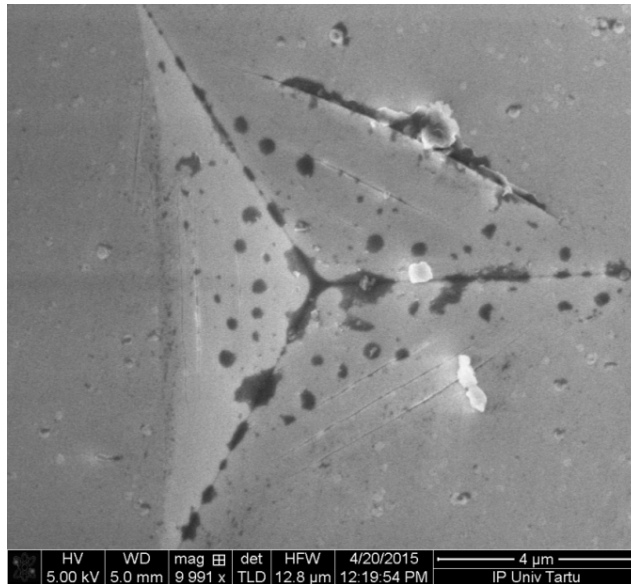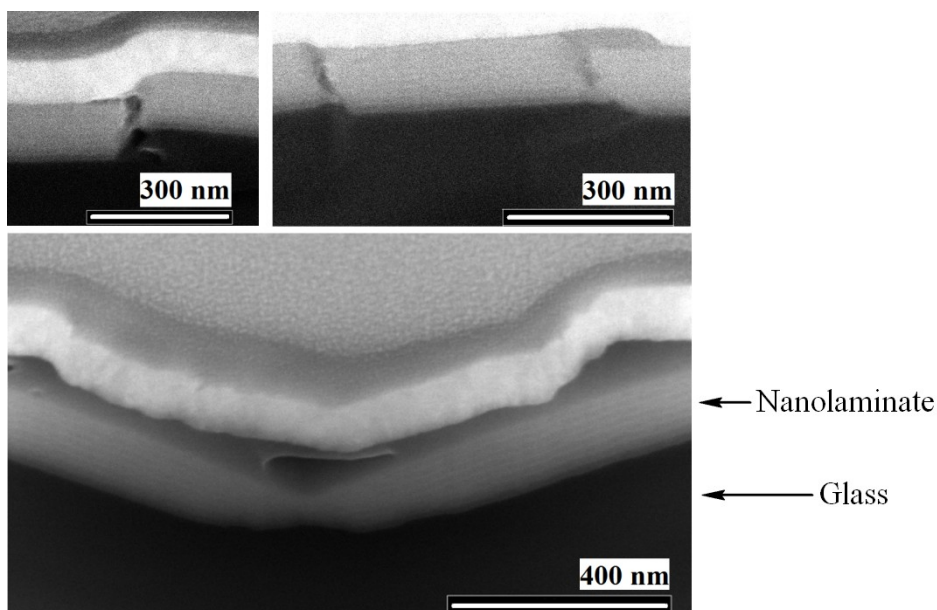

Figure 23. Top view of Ta_2O_5 + 33× (2,5 nm ZrO_2 + 2,5 nm Ta_2O_5) nanocomposite.
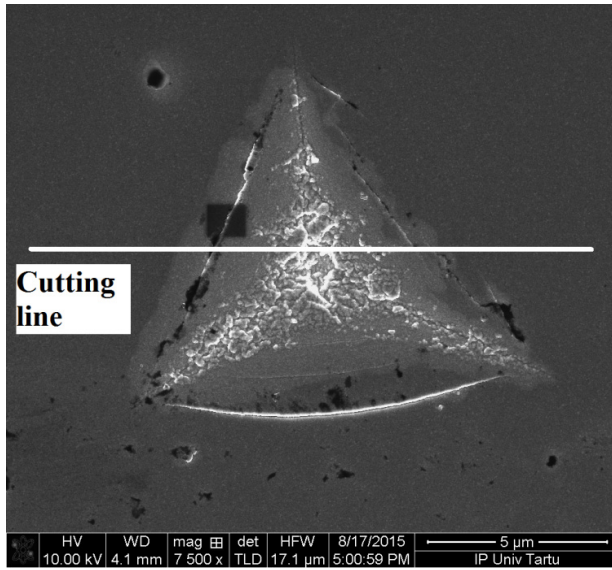
Figure 24. Top view of atomic layer deposited nanocomposite layer on glass after indentation. The white line approximately indicates the FIB cutting region.
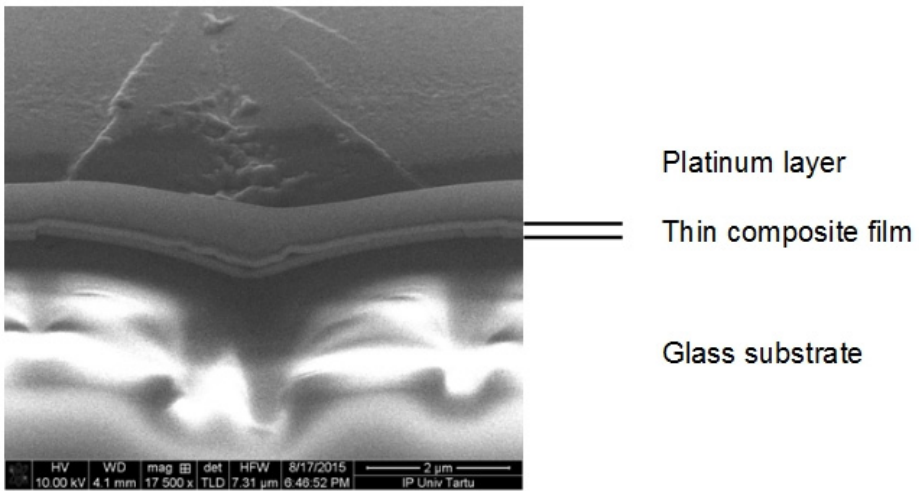
Figure 25. A FIB cut cross-section of an indentation.

Figure 26. A close-up of the FIB cut showing on top the left and right sides of the cut (indent left and right parts near surface), respectively, and structure near the indenter tip on lower panel.

The summarized instrumented nanoindentation results for hardness and reduced modulus measurements of ALD oxides and their nanocomposites on glass are shown in Table VI (standard deviations showed in parenthesis). The number in front of oxide chemical formula shows respective layer thickness in nanometers.

As it can be seen from the Table VI, the highest hardness results were obtained from single alumina and hafnia layers, while zirconia and tantala are rather similar to the glass substrate and not enhancing the properties that much. For the reduced moduli the sequence is a bit different starting with the hafnia having the highest modulus followed by alumina, tantala and zirconia as the least stiff coating.

These results, however, cannot yet be considered as conclusive. There are general trends recognized how the hardness/modulus of a nanolaminate changes compared to the change in structure, but there are also some exceptions. As a general trend – the higher the content of a harder oxide, the higher the hardness of a composite. This sounds rather straight forward logical and could be expected. But this does not hold when the results of structure of $10Ta_2O_5 + 8 \times (10HfO_2 + 10Ta_2O_5)$ is reviewed. It shows hardness rather similar to glass or tantala (both 6.7 GPa), but the modulus is considerably different from glass (67 GPa) and resembles to hafnia, especially when standard deviations are taken into account. The nanolaminate structure formula shows the ratio of single oxides to be almost 1:1, therefore both results could be expected to be in-between the properties of single oxides.

Table VI. Summarized results of nanoindentation hardness H and reduced modulus E of ALD deposited thin film oxides and their nanocomposites on glass substrate. The number before oxide chemical formula shows respective single layer thickness in nanometers.

Sample	Hardness H (st. dev.), GPa	Reduced modulus E (st. dev.), GPa
Soda-lime-glass (SLG)	6.7(0.2)	68(5)
Al_2O_3	9.5(0.5)	101(4)
HfO_2	9.1(0.7)	111(11)
ZrO_2	7.0(0.4)	86(4)
Ta_2O_5	6.7(0.2)	96(3)
$10Ta_2O_5 + 8\times (10Al_2O_3 + 10Ta_2O_5)$	7.0(0.4)	98(5)
$10Ta_2O_5 + 8\times (15Al_2O_3 + 5Ta_2O_5)$	7.4(0.5)	97(7)
$10Ta_2O_5 + 8\times (5HfO_2 + 15Ta_2O_5)$	6.7(0.2)	102(4)
$10Ta_2O_5 + 8\times (10HfO_2 + 10Ta_2O_5)$	6.8(0.2)	99(4)
$10Ta_2O_5 + 8\times (15HfO_2 + 5Ta_2O_5)$	7.4(0.3)	110(5)
$10HfO_2 + 8\times (10Ta_2O_5 + 10HfO_2)$	7.2(0.3)	103(3)
$10Ta_2O_5 + 8\times (5ZrO_2 + 15Ta_2O_5)$	6.7(0.3)	108(6)
$10Ta_2O_5 + 8\times (10ZrO_2 + 10Ta_2O_5)$	7.3(0.4)	115(4)
$10Ta_2O_5 + 8\times (15ZrO_2 + 5Ta_2O_5)$	7.3(0.7)	106(11)
$10ZrO_2 + 8\times (10Ta_2O_5 + 10ZrO_2)$	7.2(0.3)	113(9)
$7.5Ta_2O_5 + 16\times (5ZrO_2 + 5Ta_2O_5) + 2.5Ta_2O_5$	7.2(0.3)	111(6)
$5Ta_2O_5 + 33\times (2.5ZrO_2 + 2.5Ta_2O_5) + 5Ta_2O_5$	7.8(0.4)	112(4)

The second exception seems to be the last sample in the table with structure formula $5Ta_2O_5 + 33\times (2.5ZrO_2 + 2.5Ta_2O_5)$ and hardness of 7.8 GPa. For some reason the hardness, as an average, is about 10% higher than other laminates with similar tantala-zirconia ratios (7.2 GPa). On the other hand, the moduli for all ZrO_2-Ta_2O_5 laminates tend to be equally high at about 110 GPa, which is comparable to hafnia. Again, it would be expected to get moduli in-between zirconia and tantala in case of similar oxide ratios in a nanocomposite structure.

The explanation for ZrO_2-Ta_2O_5 laminates could be theorized to be in the nature of ZrO_2 crystalline structure, which partially has tetragonal phase. Zirconia is known to shift phase from tetragonal to monoclinic under mechanical stress [63 pg. 103,64]. The phase change coincides with an increase in volume ($\approx$4%) of the unit cell, which creates counteracting effect to the indenter during measurement. Of course there would be a limit of minimum mechanical stress, where the phase change starts to appear and in this case the effect could have been when the single oxide layers were about 2.5 nm thick.

As a conclusion it can be said that, most likely, nanolaminates are the simplest composite structures to produce with ALD depositing thin films with

various mechanical properties. In this case no additional process steps before ALD deposition, like in papers II and III, were required to make samples.

Atomic layer deposition of alumina on modified steel substrates

The XRD measurements did not reveal any crystalline phases of alumina or silica. The ToF-ERDA results showed the SiO_2 thickness to be around 200 nm. The CSM indentations show that deposited alumina gives distinctive rise to surface hardness and modulus (Fig. 27), but the results were poor for samples with SiO_2 bottom layer (Fig. 28), resulting about two times drop in hardness and three times in modulus in case of samples with 90 nm alumina top layer. The results, including standard deviations, are gathered in Table VII.
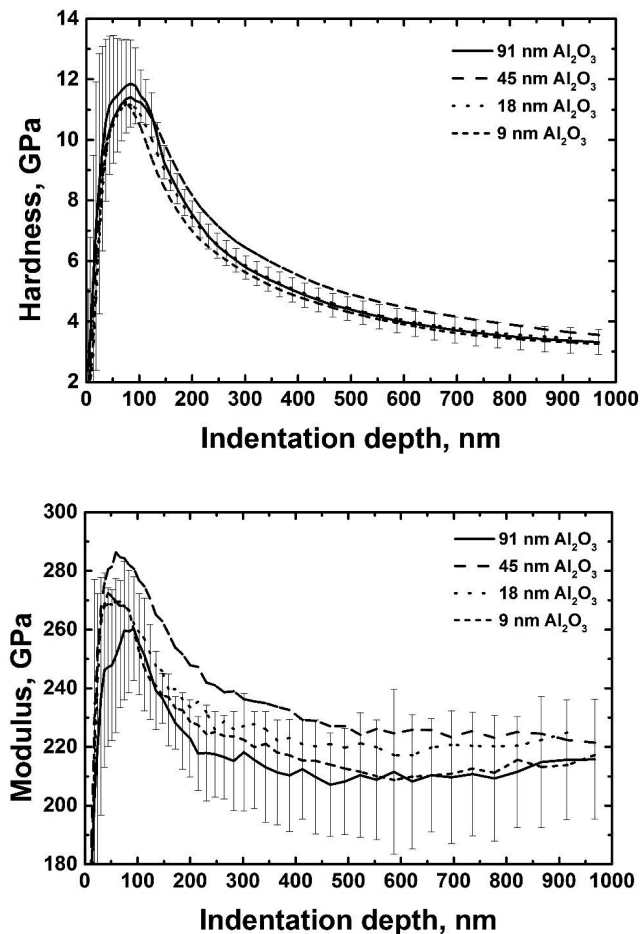
Figure 27. Hardness and modulus of steel samples coated with ALD alumina showing enhanced surface properties. The error bars, showing standard deviation, are for samples with 91 nm of alumina.
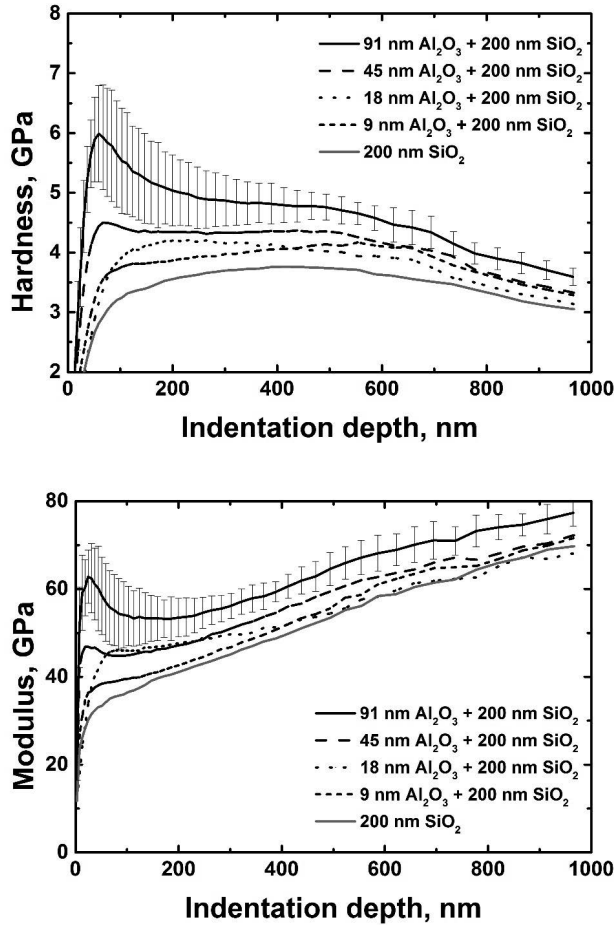
Figure 28. Hardness and modulus of steel samples coated with alumina and silica showing some enhancement of surface properties. The error bars, showing standard deviation, are for samples with 91 nm of alumina.

From Figure 27 it can be concluded that the hardness and moduli results were identical for all Al_2O_3 the samples. Therefore, the reduced hardness and modulus of alumina could be deemed to be independent from thin film thickness and had values about 11.5 GPa and 260 GPa, respectively. Figure 28 shows that the absolute values were lower for samples with silica layer only. This can be considered straight forward logical, because the alumina has higher hardness and modulus than silica and thus, silica may not enhance the surface properties as much as pure alumina coating could do. Also, according to rule of mixtures, the combination of alumina and silica would have poorer properties, which is confirmed here.

Table VII. Abridged results of instrumented nanoindentation of steel coated with Al_2O_3 and Al_2O_3-SiO_2 layers.

Coating structure		H (st. dev.), GPa	E (st. dev.), GPa
Al_2O_3, nm	SiO_2, nm		
91		11.8 (1.4)	260 (18)
45		11.4 (0.9)	286 (21)
18		11.1 (0.7)	269 (16)
9		11.2 (1.6)	272 (36)
91	200	6.0 (0.8)	62 (7)
45	200	4.5 (0.3)	46 (3)
18	200	4.2 (0.3)	46 (6)
9	200	3.8 (0.3)	39 (2)
	200	3.3 (0.3)	38 (2)

MODELING MECHANICAL PROPERTIES
OF NANOLAMINATES ON GLASS

In this chapter some models are described and later used to find the mechanical properties of thin films, which were under investigation in III (using CSM to measure properties of ALD thin films on SLG). The models under discussion are:

- The model of Puchi-Cabrera
- The model of Tuck
- Halpin-Tsai relationship

The principles of the models will be described first, followed by application and retrieved results later. The main aim of the models would be to get the closest fit to the actual CSM measurement results, especially in displacement range from measurement maximum to 170 nm, where the thin film thickness lays. If possible, a model should correlate to the CSM results in wider range, preferably up to the maximum displacement.

It should be noted that the measurement data used here correspond to reduced data. The measured properties are reduced due to the fact that during indentation not only the sample is deformed, but also the device itself. This is taken into account later after the thin film properties have determined with modeling.

Model of Puchi-Cabrera

The explanation of Puchi-Cabrera model is started with simple exponential approximation, which closely resembles it.

The idea behind exponential approximation is assumption that the measured moduli values increase exponentially up to the true value, if indenter tip displacement during indentation decreases from maximum value to 0 nm. In other words, the indentation process is interpreted in reverse order. The tip is first seen to be positioned in final depth, results showing the values for the final depth and we start to pull out the tip. As the depth decreases, the thin film modulus should start to influence the results increasingly, the influence of the substrate is diminishing step-by-step until at the 0 nm displacement, the modulus value should correspond to the modulus of the coating. Starting interpreting from displacement of 0 nm, it could be said that a property is exponentially decaying. The overall measured property is considered as the sum of that of the glass and the increase given by the thin film to the substrate. The applied equation is then:

$$P_c = P_{gl} + \frac{P}{e^{hc}} , \qquad \text{Equation 51}$$

where P_c is the composite property, P_{gl} is the property of the glass, P is the increase or difference (compared to the substrate) caused by the coating, h is the displacement and C is the fitting parameter. The Eq. 51 can be written also as:

$$P_c = P_{gl} + \frac{(P_{tf} - P_{gl})}{e^{hC}}, \qquad \text{Equation 52}$$

where P_{tf} is the property of the thin film.

Equation 52 is in principle analogous to model for coating hardness calculation proposed by Puchi-Cabrera (P-C) [65]:

$$H = H_S + \frac{(H_C - H_S)}{e^{kZ_R^n}}, \qquad \text{Equation 53}$$

where H is the composite hardness, H_S is the substrate hardness, H_C is the coating hardness and Z_R is the relative thickness (indentation depth divided by coating thickness). The constants k and n are said to be characteristic to the materials and related indentation process and can be used to get a good fit with measurement results. The main difference in Eq. 52 and Eq. 53 is how the fitting constants are taken into account. In simple exponential equation the $n=1$ and consequently C is k divided by coating thickness. Therefore, it can be said that the exponential approximation is a special case of Puchi-Cabrera model and it might be up to measurement results, which could be applied.

The results of P-C and exponent models applied on alumina measurement results is shown on Figure 29. It can be seen that the models describe the data points very well throughout the whole displacement range. According to Puchi-Cabrera, the correlation coefficient for P-C model and measurement data is often 0.99 or better.

It can be seen that the two calculated lines are not distinguishable and give almost identical results. This was later confirmed for all the other samples and therefore it was concluded that when modeling CSM results with Puchi-Gabrera formula, it is safe to take $n=1$ and use k to achieve a fit. If displacement is 0, the results for P-C and exponential model are the same.

Figure 30 shows the effect of k to the fit. Using $k=1$ instead $k=2$ will give a line well above the measured data points and $k=3$ gives line below the points. (The line following the points is calculated as exponential approximation.) For all three k values the fit was still very good at greater indentation depths in the range from about 600 to the end.
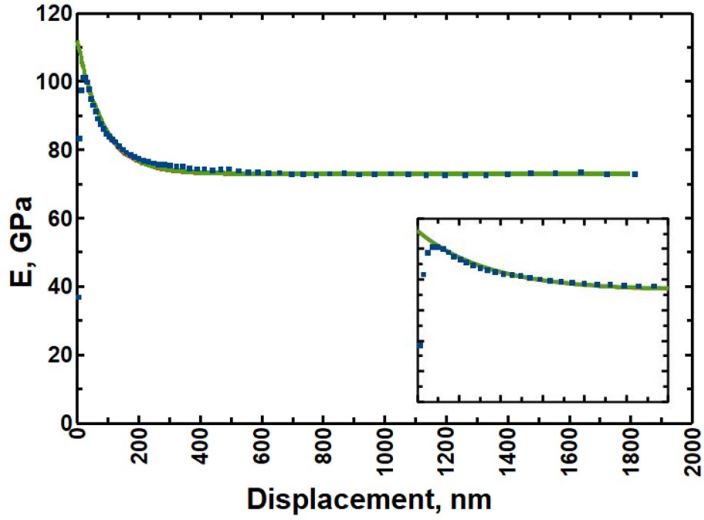
Figure 29. Calculated lines for simulating modulus measured points of alumina on glass substrate according to P-C model and exponential approximation, where *n=1* and *k=2*. The constant *C* has been taken *C=0,012* for the exponent function. The inset shows graphs in the displacement range 0–300 nm.
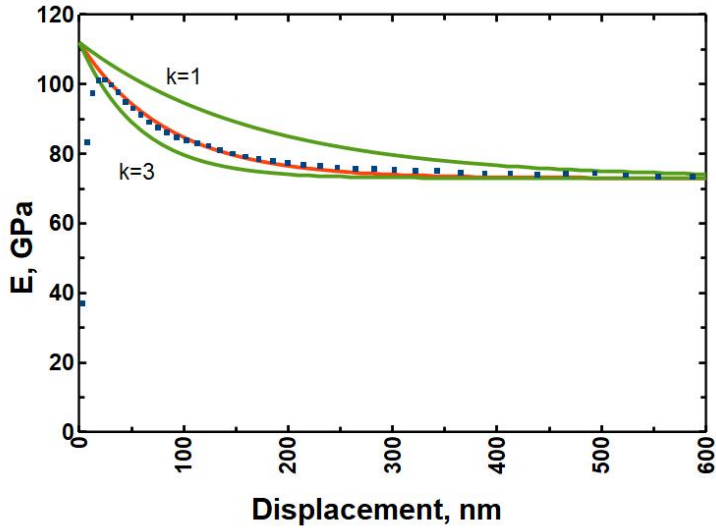
Figure 30. The effect of *k* in P-C model applied to alumina measurements: *k=1* (upper panel) and *k=3* (lower panel); *n=1* for both cases. The line following the points is calculated using exponential approximation.

Figure 31 demonstrates the effect of *n* to the fit. Using *n=0,5* instead *n=1* will give a line well above the measured data points and *n=1,5* gives line below the points. (The line following the points is calculated as exponential approximation.) For all three *n* values the fit was still very good at greater indentation depths in the range from about 600 to the end.
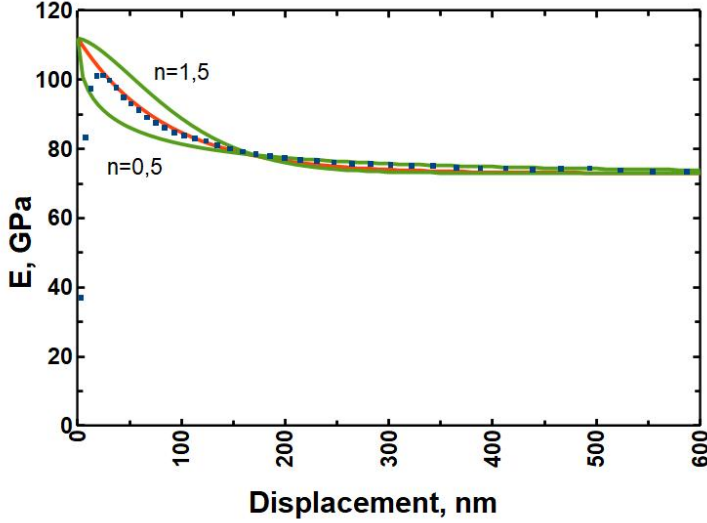
Figure 31. The effect of *k* in P-C model applied to alumina measurements: *n=0,5* (upper panel) and *n=1,5* (lower panel); *k=2* for both cases. The line following the points is calculated using exponential approximation.

There is actually a discrepancy built in the presented last three images compared to Eq. 52 and Eq. 53 in the theory. The equations note that the glass as a substrate property should be introduced into the formula, which is taken here as 69 GPa (for reduced modulus of glass) as mentioned in previous sections. This also means that the modeling results should show values near 69 GPa, but in fact are higher. For most cases it is somewhere near 72 GPa to get a good fit with actual measurements and models and for pure tantala and zirconia (and mixtures thereof) the base value is near 83 GPa. The higher values of properties can be argued to be the result of the combined properties of substrate and thin film. It was concluded that the substrate property in P-C model (Eq. 53) should be redefined as a material base property:

$$P = P_{base} + \frac{(P_{tf} - P_{base})}{e^{kz_R^n}} \qquad \text{Equation 54}$$

The P_{base} is defined as the average value of a property between displacements 800–1800 nm. In case there was a creeping rise in a property, the lowest value after maxima were chosen as the baseline. This kind of selection might not be absolutely correct, because there might be some hindering effects like pile up,

phase changes in material or gradient changes in a property from surface to inside. Pile up means that some material would rather come out from sample and surround indenter tip, which results in increase of force needed to deform the additional material. This tends to show on graphs as ever increasing property value being highest in the final indentation depth. If a phase change occurs during indentation in substrate or coating, it can alter the results showing higher or lower values depending on the formed phase properties.

Taking into account the given explanations, the thin film properties where calculated using Eq. 54 and are presented in Table VIII. The parameters in model were changed to get the lowest possible property value and visibly the best fit in the whole displacement range.

Table VIII. Calculated thin film reduced properties according to model derived by Puchi-Cabrera. Thin film thickness 170 nm; $n=1$ and $k=2$ for all samples, if not noted otherwise.

Sample	P-C	
	E, GPa	H, GPa
Al_2O_3	112	11.4[a]
HfO_2	128	11.1[b]
ZrO_2	91	7.2
Ta_2O_5	104	7.0
$10Ta_2O_5 + 8\times (10Al_2O_3 + 10Ta_2O_5)$	109	7.5
$10Ta_2O_5 + 8\times (15Al_2O_3 + 5Ta_2O_5)$	113	8.2
$10Ta_2O_5 + 8\times (5HfO_2 + 15Ta_2O_5)$	116	6.8
$10Ta_2O_5 + 8\times (10HfO_2 + 10Ta_2O_5)$	113	7.1
$10Ta_2O_5 + 8\times (15HfO_2 + 5Ta_2O_5)$	125	8.4
$10HfO_2 + 8\times (10Ta_2O_5 + 10HfO_2)$	115	7.7
$10Ta_2O_5 + 8\times (5ZrO_2 + 15Ta_2O_5)$	121	6.8
$10Ta_2O_5 + 8\times (10ZrO_2 + 10Ta_2O_5)$	126[c]	8.0
$10Ta_2O_5 + 8\times (15ZrO_2 + 5Ta_2O_5)$	114[d]	8.0
$10ZrO_2 + 8\times (10Ta_2O_5 + 10ZrO_2)$	123[e]	7.6
$7.5Ta_2O_5 + 16\times (5ZrO_2 + 5Ta_2O_5)$ $+ 2.5Ta_2O_5$	125	7.6
$5Ta_2O_5 + 33\times (2.5ZrO_2 + 2.5Ta_2O_5)$	126	8.9

[a] $k=1.7$, [b] $k=1.3$, [c] $k=1.4$, [d] $k=1.2$, [e] $k=1.6$

Model of Tuck

This model was proposed by Tuck *et. al.* in 2000 [66]. Its expression and content is similar to Puchi-Cabrera:

$$H_c = H_S + \frac{(H_F - H_S)}{1 + kZ_R^X}, \qquad \text{Equation 55}$$

where H_c is the composite hardness, H_s is the substrate hardness, H_f is film hardness, Z_R is the relative thickness, k and X are fitting parameters with same meaning as in P-C model. The main difference between these two models can be seen on Figure 32.
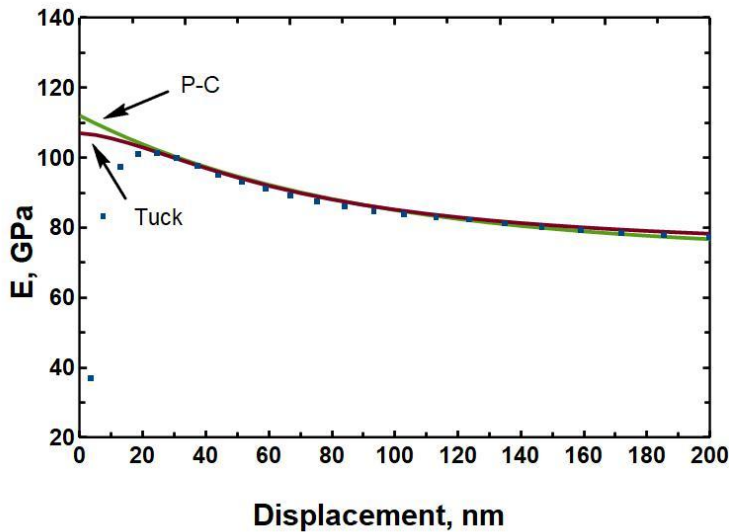
Figure 32. Image visualizing the difference of models of Tuck and Puchi-Cabrera during first nanometers of indentation. The sample is alumina thin film on glass.

Mostly the models of P-C and Tuck coincide (Fig. 33), but the latter shows lower drop in properties, when a measurement has been commenced. On the other hand, it gives lower values at 0 nm of displacement. The lower initial change in properties indicates that there could be a region where the substrate influence could be negligible. (This region will be discussed in depth later.)

The results according to Tuck were calculated at similar conditions and are summarized in Table IX.
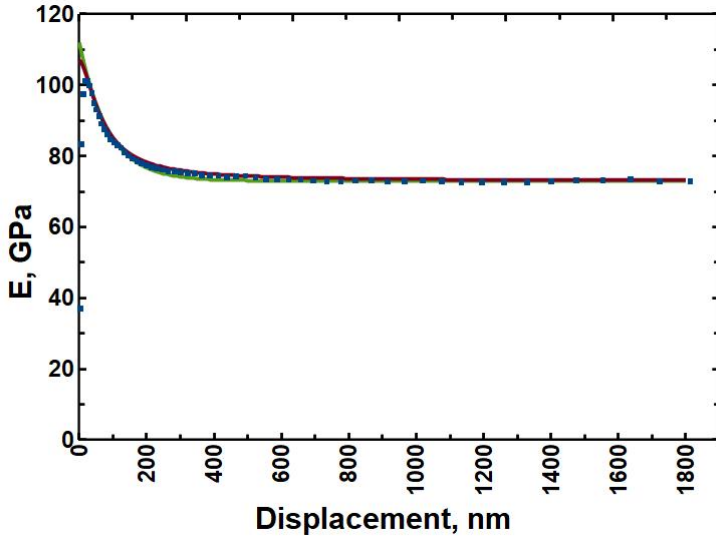
Figure 33. Models of P-C and Tuck applied to measurement data of alumina on glass sample.

Table IX. Results of moduli and hardnesses according to Tuck including respective values for k and X.

Sample	Tuck		k;X	
	E, GPa	H, GPa	E	H
Al_2O_3	107	11.3	4.2;1.6	4.2;1.6
HfO_2	125	10.7	4.2;1.6	2.4;1.8
ZrO_2	89	7.2	5.5;1.6	4.2;1.6
Ta_2O_5	103	7.0	4.2;1.6	4.2;1.6
$10Ta_2O_5 + 8\times (10Al_2O_3 + 10Ta_2O_5)$	105	7.4	4.2;1.6	4.2;1.6
$10Ta_2O_5 + 8\times (15Al_2O_3 + 5Ta_2O_5)$	109	8.0	5.2;1.7	6.0;2.1
$10Ta_2O_5 + 8\times (5HfO_2 + 15Ta_2O_5)$	110	6.8	4.2;1.6	6.0;2.1
$10Ta_2O_5 + 8\times (10HfO_2 + 10Ta_2O_5)$	107	7.1	4.2;1.6	3.0;2.5
$10Ta_2O_5 + 8\times (15HfO_2 + 5Ta_2O_5)$	119	7.8	4.2;1.6	2.5;2.0
$10HfO_2 + 8\times (10Ta_2O_5 + 10HfO_2)$	112	7.7	4.2;1.6	6.0;2.1
$10Ta_2O_5 + 8\times (5ZrO_2 + 15Ta_2O_5)$	119	6.7	5.5;1.6	4.2;1.6
$10Ta_2O_5 + 8\times (10ZrO_2 + 10Ta_2O_5)$	122	7.8	3.0;1.7	4.2;1.6
$10Ta_2O_5 + 8\times (15ZrO_2 + 5Ta_2O_5)$	112	7.9	2.0;1.7	4.2;1.6
$10ZrO_2 + 8\times (10Ta_2O_5 + 10ZrO_2)$	120	7.4	4.0;1.7	4.2;1.6
$7.5Ta_2O_5 + 16\times (5ZrO_2 + 5Ta_2O_5)$ $+ 2.5Ta_2O_5$	120	7.5	5.5;1.6	4.2;1.6
$5Ta_2O_5 + 33\times (2.5ZrO_2 + 2.5Ta_2O_5)$	119	8.3	4.0;1.7	4.0;2.1

Modeling with Halpin-Tsai relationship

Previously discussed Halpin-Tsai relationship is used as possible model to determine the thin film properties. As a reminder, the equations to be used are (similar to Eq. 25):

$$P = P_{gl}\left(\frac{1+\xi\chi v_{tf}}{1-\chi v_{tf}}\right) \qquad \text{Equation 56}$$

and (similar to Eq. 26):

$$\chi = \frac{P_{tf}-P_{gl}}{P_{tf}+\xi P_{gl}}, \qquad \text{Equation 57}$$

where P_{gl} is the property of glass, P_{tf} is the property of thin film and v_{tf} is the volume fraction of thin film. Here the main goal is first to find ξ (Eq. 27) and then use the value for calculating hardness and modulus at other displacements. The calculations for volume fractions are given by the rule of mixture model.

It has turned out that the term ξ is not constant throughout the whole displacement range, varying from about 0 to 11 for alumina-glass system and occasionally having negative values. Therefore, the Halpin-Tsai relationship is not applicable on these CSM measurement data. Consequently, other models based on Halpin-Tsai relationship are also (partly) discredited and have to be excluded.

Determination of critical displacement using rule of mixture

The critical displacement is indentation depth, where the substrate starts to affect the measurement results. In other words, before reaching critical displacement, the measured properties can be assimilated to the coating only.

The Reuss bound is taken here as the starting point (Eq. 14):

$$\frac{1}{E_c} = \frac{v_{tf}}{E_{tf}} + \frac{v_{gl}}{E_{gl}}$$

where E_c is the composite modulus, E_{tf} is the thin film modulus and E_{gl} is the glass (substrate) modulus. The resultant E_c is considered at every measurement point as mixture of the coating-substrate system and accordingly Reuss bound is applied, because the measurements have been done transverse to the deposited layers. The moduli values for each system are taken from models of Puchi-Cabrera and Tuck (Table VIII and Table IX).

The principles for calculating volume fractions is as follows. The total composite volume V_c can be calculated as the sum of indented thin film volume fraction V_{tf} and glass substrate V_{gl}, in accord with Eq. 11:

$$V_c = V_{tf} + V_{gl}$$

For Berkovich triangular pyramid indenter geometry, with ideal shape (*i.e.* no blunting of the tip or similar effects), can be written:

$$V_c = 8.187 \times h_c^3 \,,$$
<div align="right">Equation 58</div>

where h_c is the total indentation depth (displacement). Of course, the total depth is the sum of the displacement into the thin film h_{tf} and the glass h_{gl}.

$$h_c = h_{tf} + h_{gl}$$
<div align="right">Equation 59</div>

Taking into account Eq. 59 and the 3rd power correlation of the volume and the depth, the volume of glass substrate can be calculated as:

$$V_{gl} = 8.187 \times \left(h_c^3 - h_{tf}^3\right)$$
<div align="right">Equation 60</div>

The volume for thin film can be now calculated as the difference:

$$V_{tf} = V_c - V_{gl} = 8.187 \times \left(h_c^3 - h_{gl}^3\right)$$
<div align="right">Equation 61</div>

The volume fractions are calculated according to Eq. 10:

$$v_{tf} = V_{tf}/V_c$$
<div align="right">Equation 62</div>

and

$$v_{gl} = V_{gl}/V_c$$
<div align="right">Equation 63</div>

The v_{tf} and v_{gl} can be expressed also using derivation of Eq. 11 (the sum of all volume fractions is 1, thus, in two-component system, one fraction can be obtained by subtracting the other part from 1). Also, it is assumed that the material is well adhered to the tip and the pre-indentation surface level is maintained, so that the material plastic deformation is directly relatable to the tip geometry (volume) and displacement from surface initial level.

The values for displacements are different from the measurement values. The values for h_c are taken as x-axis values and were up to 1800 nm (about equal to that of the measurement maximum). The values for h_{gl} is taken in accord with the principle that the influence of mechanical stresses start to have an effect after the influence on thin film is already in effect. Therefore, the values of h_{gl} are smaller or "lagging" behind compared to h_{tf}. Starting with the modeling again from the end of the CSM graph, it has turned out that the relationship between h_{tf} and h_{gl} is linear. In other words, there could be a situation where the indenter is already affecting the thin film, but there is no influence in the substrate. The displacement difference calculated from those two phenomena is

considered as the critical displacement depth t_c. This was later confirmed in calculations, where the h_{gl} in the model was already 0, but the h_{tf} was still reducing towards 0. The negative h_{gl} values is neglected in this model.

The choice of baseline is different compared to previous models. The baseline for ROM is the respective property of glass, *i.e.* modulus of 69 GPa and hardness of 6,6 GPa. Changing the value from 69 to 73 GPa will give the baseline suitable for previous models (dashed line in Fig. 34). The moduli values from Tuck were used as E_{tf} input, because these gave higher t_c values compared to P-C model and will be considered as the possible maxima.

To get the horizontal line, corresponding only to the substrate, the linear relationship between h_{tf} and h_{gl} has to be expressed as:

$$h_{tf} = 1 \times h_{gl} - 0$$

Equation 64

This means that the total volume of indenter in material is equal to the volume of indented glass. The volume of indented thin film is the difference between total volume and volume of indented glass, which results in 0 in this case. This can happen only if the pure substrate is indented. It would be logical to presume that the properties of the homogeneous substrate would be constant and thus, give a graph with 0 slope. Therefore, a value other than 0 could not be expected for intercept.
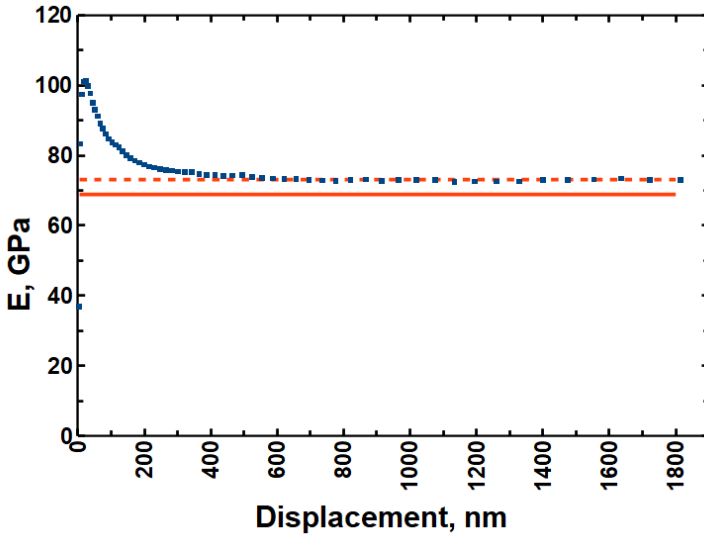
Figure 34. The baseline for ROM: the dashed horizontal line shows the 73 GPa level, which would be suitable for previous models and the lower, 69GPa value, indicates the one used in rule of mixture model. The sample is Al_2O_3-SLG.

The next step was to manually assign the slope to position the model to the CSM values in-between 800–1800 nm. A value of 0.96 was suitable for Al$_2$O$_3$-SLG system (dashed line on Fig. 35). This, in principle, has the same effect as suggesting a substrate modulus of 73 GPa in the rule of mixture.

Next was to increase the intercept values step-by step until best fit line to CSM graph shape was obtained for model. The goal was to set the lowest value, which corresponds to the situation during indentation where the influence of glass would inchoate. It would be logical to expect the glass influence to start as close to 0 displacement as possible. The result is shown in Figure 35 as continuous line.
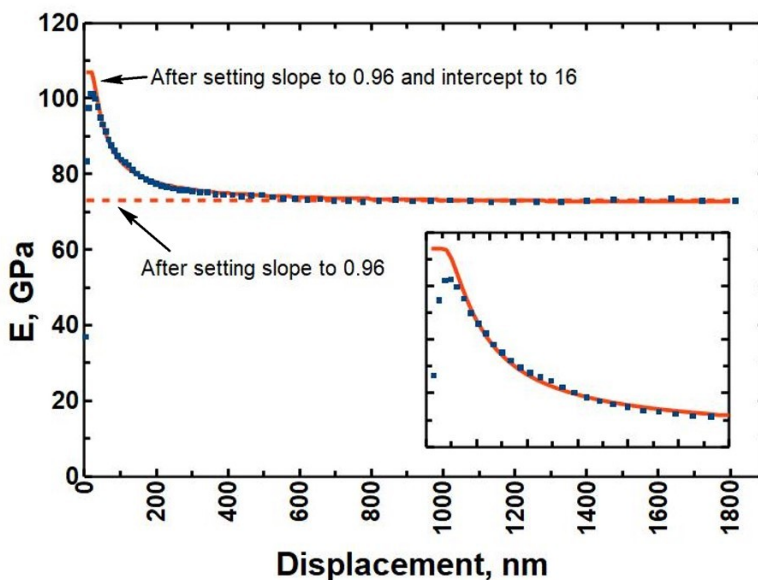
Figure 35. Evolution of rule of mixture model of Al$_2$O$_3$-SLG system with adjusted parameters. The inset shows data from 0 to 300 nm. The linear equation was $h_{tf}=0.96h_{gl}-16$.

It can be concluded that the glass substrate starts to have some effect on measurements after 16 nm of displacement.

The same procedure was done with other moduli data and the results are summarized in Table X.

It has been pointed out that, depending on the property differences of the coating and substrate, this region could be up to 20% of the thin film thickness, where the substrate does not affect the coating properties [67,68]. From another side, this means that it is possible to determine the displacement range, where the substrate effect is 0. This was later confirmed in calculations and as it can be seen from Table X the critical values are well below the displacements, where the maxima during CSM measurements appeared. Therefore, the value at maxima does not correspond to the real thin film property.

Table X. The critical displacements t_c for ALD thin films on glass substrate as calculated from ROM model using E_{tf} moduli from model of Tuck as input.

Sample	t_c, nm
Al_2O_3	16
HfO_2	19
ZrO_2	12
Ta_2O_5	12
$10Ta_2O_5 + 8\times (10Al_2O_3 + 10Ta_2O_5)$	16
$10Ta_2O_5 + 8\times (15Al_2O_3 + 5Ta_2O_5)$	15
$10Ta_2O_5 + 8\times (5HfO_2 + 15Ta_2O_5)$	21
$10Ta_2O_5 + 8\times (10HfO_2 + 10Ta_2O_5)$	18
$10Ta_2O_5 + 8\times (15HfO_2 + 5Ta_2O_5)$	19
$10HfO_2 + 8\times (10Ta_2O_5 + 10HfO_2)$	18
$10Ta_2O_5 + 8\times (5ZrO_2 + 15Ta_2O_5)$	14
$10Ta_2O_5 + 8\times (10ZrO_2 + 10Ta_2O_5)$	20
$10Ta_2O_5 + 8\times (15ZrO_2 + 5Ta_2O_5)$	22
$10ZrO_2 + 8\times (10Ta_2O_5 + 10ZrO_2)$	16
$7.5Ta_2O_5 + 16\times (5ZrO_2 + 5Ta_2O_5)$ $+ 2.5Ta_2O_5$	15
$5Ta_2O_5 + 33\times (2.5ZrO_2 + 2.5Ta_2O_5)$	16

The range possibly depends on the fact how different are the thin film (ALD oxide) and substrate (glass) properties, thus, different values should be expected for different coating-substrate systems, which seems to be rather straight forward logical assumption. From Table X it can be seen that the *tc* values are mostly about 10% of the thin film thickness of 170 nm or less and are well below 20% margin. This indicates that the results from ROM correspond to expectable results.

Calculation of true thin film properties

So far, the thin film properties have been shown as reduced properties. It might be of some interest to know the true (absolute) properties of the films.

To do that, the deformation of indenter tip material (diamond, ν_i=0.07, E_i=1140 GPa) was taken into account according to:

$$\frac{1}{E_r} = \frac{1-\nu_i^2}{E_i} + \frac{1-\nu_f^2}{E_f}$$

The final results for moduli can be seen in Table XI.

Table XI. Absolute values of thin film moduli (in GPa). For SLG: $\nu=0.22$ and $E_{tr}=70$ GPa. The Poisson coefficient for all thin films was $\nu=0.25$.

Sample	P-C	Tuck	E_{tr} values	
Al_2O_3	112	107	116	110
HfO_2	128	125	135	131
ZrO_2	91	89	92	90
Ta_2O_5	104	103	107	106
$10Ta_2O_5 + 8\times (10Al_2O_3 + 10Ta_2O_5)$	109	105	113	108
$10Ta_2O_5 + 8\times (15Al_2O_3 + 5Ta_2O_5)$	113	109	117	113
$10Ta_2O_5 + 8\times (5HfO_2 + 15Ta_2O_5)$	116	110	121	114
$10Ta_2O_5 + 8\times (10HfO_2 + 10Ta_2O_5)$	113	107	117	110
$10Ta_2O_5 + 8\times (15HfO_2 + 5Ta_2O_5)$	125	119	131	124
$10HfO_2 + 8\times (10Ta_2O_5 + 10HfO_2)$	115	112	120	116
$10Ta_2O_5 + 8\times (5ZrO_2 + 15Ta_2O_5)$	121	119	126	124
$10Ta_2O_5 + 8\times (10ZrO_2 + 10Ta_2O_5)$	126	122	132	128
$10Ta_2O_5 + 8\times (15ZrO_2 + 5Ta_2O_5)$	114	112	118	116
$10ZrO_2 + 8\times (10Ta_2O_5 + 10ZrO_2)$	123	120	129	125
$7.5Ta_2O_5 + 16\times (5ZrO_2 + 5Ta_2O_5) + 2.5Ta_2O_5$	125	120	131	125
$5Ta_2O_5 + 33\times (2.5ZrO_2 + 2.5Ta_2O_5)$	126	119	132	124

It can be seen that for most cases the average values are 4–6 GPa higher and compared to as measured maxima, the values were mostly 10–15 GPa higher. The deviation of ±0.05 from suggested Poisson coefficient would give about ±3 GPa change in moduli.

Predicting properties of nanolaminates using single ALD oxide properties and Reuss bound

This chapter is devoted to try Reuss bound to predict modulus of lamina built with two different oxides using moduli of single oxides derived from Puchi-Cabrera model.

The volume fraction calculations were based on the suggested layer thicknesses expressed in respective equations indicating the structure. The results are gathered in Table XII.

It can be seen that the Reuss bound predictions for nanolaminates of two oxides are quite close to the values derived from Puchi-Cabrera. The largest disparity was in ZrO_2 laminates, which showed remarkably higher values compared to single oxides and at some points resembled to the modulus of hafnia. The exact explanation still stays hypothetical and open.

Table XII. Volume fractions of oxides in laminates and respective prediction values.

Sample	v(Ta_2O_5)	v(oxide)	P-C	Reuss
Al_2O_3			112	
HfO_2			128	
ZrO_2			91	
Ta_2O_5			104	
$10Ta_2O_5 + 8\times (10Al_2O_3 + 10Ta_2O_5)$	0.529	0.471	109	108
$10Ta_2O_5 + 8\times (15Al_2O_3 + 5Ta_2O_5)$	0.294	0.706	113	110
$10Ta_2O_5 + 8\times (5HfO_2 + 15Ta_2O_5)$	0.765	0.235	116	109
$10Ta_2O_5 + 8\times (10HfO_2 + 10Ta_2O_5)$	0.529	0.471	113	114
$10Ta_2O_5 + 8\times (15HfO_2 + 5Ta_2O_5)$	0.294	0.706	125	120
$10HfO_2 + 8\times (10Ta_2O_5 + 10HfO_2)$	0.471	0.529	115	115
$10Ta_2O_5 + 8\times (5ZrO_2 + 15Ta_2O_5)$	0.765	0.235	121	101
$10Ta_2O_5 + 8\times (10ZrO_2 + 10Ta_2O_5)$	0.529	0.471	126	97
$10Ta_2O_5 + 8\times (15ZrO_2 + 5Ta_2O_5)$	0.294	0.706	114	94
$10ZrO_2 + 8\times (10Ta_2O_5 + 10ZrO_2)$	0.471	0.529	123	97
$7.5Ta_2O_5 + 16\times (5ZrO_2 + 5Ta_2O_5)$ $+ 2.5Ta_2O_5$	0.529	0.471	125	97
$5Ta_2O_5 + 33\times (2.5ZrO_2 + 2.5Ta_2O_5)$	0.515	0.485	126	97

Remarks on the errors and uncertainties

The errors, which could appear during the atomic layer deposition and nano-indentation, are shortly discussed in this chapter.

ALD related errors could rise from deposition chamber temperature or pulse timings. For instance, the crystallinity of ALD thin films could change due to temperature. The errors were marginal for pulse lengths considering that the ALD by definition requires pulse lengths to achieve growth through saturated surfaces and the pulse lengths in every deposition were at least twice the length needed. The temperature measurement accuracy and stability was kept at ±1% or lower. This avoids any possible deposition in regions, where, for instance, thin film phase composition could be altered.

Somewhat more problematic and higher errors are related to instrumented nanoindentation. There are a lot of possible accuracy problems, which could appear during indentation and are related to one or more sources [69]:

- Properties of the sample
- Properties of the indenter
- Device properties
- Models used for data manipulation
- Temperature changes and drifts

- Contact profile, including pile-up and sink-in
- Surface forces and adhesion
- Indentation size effect

It would be beneficial to know some properties of a sample in advance, because it could change the ways the data are collected or interpreted. The material could behave like elastic-plastic material, brittle or loading could induce some property changes. The deformation could be more or less time dependent. The materials tend to act differently if there is no or some crystallinity or the sample is fully crystalline. This can even change during indentation and, thus, give erroneous results if not taken into account.

Additionally, the sample could have considerable surface roughness. The indenter will become in contact with the higher asperities first and gradually conforms with the surface. The overall effect is like the sample has a layer of more compliant material on top of it.

Likely the most important property related to indenter is its shape. This is calibrated usually using fused silica as it deforms during indentation similarly to the assumptions of theoretical models. There is no remarkable sink-in or pile-up effects. During the calibration the silica sample is indented in a range of depths and a property, for instance the hardness, should turn out the same for all depths.

Another phenomenon which has to be taken into account is the fact that the indenter tip material itself will deform to some extent during indentation. In this work this was corrected in the chapter of calculating absolute thin film properties.

The build of the indentation device can affect the measurements due the deformations in sample holder and other parts of the device. This is called device compliance. If lower value of compliance is used instead of the correct value, the results would be lower for both, modulus and hardness. If higher value is used, the result would be also higher. Device compliance has more influence on modulus than hardness and is usually larger for higher loads and stiffer samples.

The role of theoretical models used for calculating properties is quite crucial. One example is the model of Oliver and Pharr, where they proposed power law over linear to calculate the contact stiffness. This enhanced vastly the accuracy of final results.

In the last part of discussion of this work, several models were used to derive the properties responding only to the ALD thin films. One basis for all those models was the interpretation from the end towards the beginning. This was done because the measurement data points had lower standard deviations in the end, about ±3 GPa. This is believed to be the accuracy of the models, because the data points for models could be changed, according to measurements, to have values in-between those margins and would end up higher or lower modulus or hardness value respectively. (The measured deviations were shown in respective original works.)

Materials can expand or contract due to temperature change. If this happens during indentation, the results would be altered. This is because the temperature alters the apparent contact depth and area.

There are materials, which deviate from ideal or easily modeled material. For instance, the contact area would differ for a material, which tends to come out from the sample and gather around (pile-up) the indenter tip. This kind of material are usually soft, have high ratio of elastic modulus to yield stress and do not strain harden. The contact area would be different also for opposite situation, where the material would not be around the tip tightly, showing lower contact area and therefore over-estimating hardness, for instance.

The adhesion might interrupt the measurements if the loading forces are below several tens of micronewton. In that case the adhesive forces between tip and sample atoms might have relatively large effect on applied/measured force and therefore have to be taken into account.

Indentation size effect (IZE) can play remarkable role in measurement error. This usually occurs when the indentation depths are very shallow, below 1 micrometer. It is often observed during indenting metals and is related to indentation volume and dislocation count in the volume. The relation to dislocations is quite evident as the IZE is more significant in annealed samples opposed to cold-worked ones.

Conclusions on experimental and discussion

Experiments showed that the easiest way to gain a compact nanocomposite using ALD would be to deposit a laminate structure, but other possibilities to produce nanocomposites (*i. e.* nanoparticle or nanofiber filled) exist also.

The instrumented nanoindentation showed that deposited thin films are relatively hard and elastic. Using nanoparticle filling in composite structure showed some enhanced properties compared to viewed pure ALD oxides.

Continuous stiffness measurement technique proved to be useful at measuring mechanical properties of nanolaminate coatings and the results could be analyzed using several theoretical models (exponential, Puchi-Cabrera, Tuck, rule of mixture), but not all viewed models were suitable (Halpin-Tsai relationship).

According to models, using softer substrate for a coating would lower its mechanical characteristics and the true properties tend to possess higher values.

Somewhat abnormal results were gained with ZrO_2 nanolaminates, in which case the composite structure showed enhanced properties compared to the both consistent single oxides. This still leaves room for research on the topic.

Overall, the results indicated that the ALD thin films have different hardness and/or modulus than seen on macroscopic counter parts. It is important, for example, in the sense that if a harder than a metal (*i. e.* steel), but with similar modulus, ceramic coating is needed, ALD could give a solution. For instance, surface passivation or corrosion protection of device parts with E≈110 GPa (*i. e.* some Al-alloys) under mechanical stresses could be coated with alumina, which has similar modulus.

SUMMARY

In this study atomic layer deposition combined with several other techniques was used to produce nanostructured composites. Three structure types were realized: fiber or particle filled and laminated structures. Mechanical properties (modulus and hardness) of composites were tested using instrumented nanoindentation. The results were analyzed in the context of several theoretical models where reasonable.

Tests have shown that it is probably the easiest to prepare ALD laminated composites, where preparations were simple and compact sample was obtained without additional work techniques. The remaining types of structures likely need further research and optimization for best results.

The elastic modulus measurements showed that the ALD films were not very rigid. For example, an amorphous Al2O3 was about 3 times less than the modulus of corundum-type Al_2O_3 (*i. e.* about 110 GPa *versus* ≈340 GPa). HfO_2, Ta_2O_5, ZrO_2 modules were also lower compared to bulk objects in macroscale.

Elastic moduli of the composite laminates were intermediate between the values of the pure oxides, with the exception of ZrO_2-Ta_2O_5 nanolaminates, in which case the moduli were larger compared to pure oxides. The exact causes of the phenomenon are still unaccounted for.

The hardness of pure Al_2O_3 and HfO_2 were nearly two times harder than soda-lime-glass (11–12 GPa and 6.7 GPa, respectively). Zirconium, and tantalum oxide were close to the hardness of glass (≈7 GPa).

Results suggest that ALD oxide films are relatively hard materials and they could be matched to the different elastic moduli of other materials using various composite structures. The latter may be useful, for example, if it is desired to use the ALD films on metals or alloys (*e.g.* for corrosion protection). ALD films also allow to change mechanical properties of material surfaces that may be necessary in, for example, micro- or nanoelectromechanical (NEMS/MEMS) devices.

SUMMARY IN ESTONIAN

Aatomkihtsadestatud kilede ja nanokomposiitide mehaanilised omadused

Käesolevas töös kasutati aatomkihtsadestamist koos teiste töövõtetega nanostruktuursete komposiitide valmistamiseks. Töö käigus valmistati kolme erinevat tüüpi komposiite: kiud- või pulbertäitega ning laminaatsed komposiidid. Saadud materjalidel mõõdeti instrumentaalse nanoindenteerimisega elastsusmoodulid ja kõvadused. Mõõtmistulemusi analüüsiti kasutades erinevaid teoreetilisi mudeleid.

Katsed näitasid, et tõenäoliselt on kõige lihtsam valmistada laminaatstruktuuriga komposiite, mille korral ettevalmistused olid lihtsamad ja lisatöövõtteid kompaktse näidise saamiseks ei olnud vaja kasutada. Ülejäänud tüüpi struktuuride korral on tõenäoliselt vaja lisauuringuid ja optimeerimist parimate tulemuste saavutamiseks.

Elastsusmoodulite mõõtmine näitas, et aatomkihtsadestatud kiled ei ole väga jäigad. Näiteks oli amorfse Al_2O_3 moodul umbes 3 korda väiksem korundi-tüüpi Al_2O_3-st ($\approx$110 GPa vs $\approx$340 GPa). HfO_2, Ta_2O_5, ZrO_2 moodulid olid samuti väiksemad makroskoopiliste objektidega võrreldes.

Komposiitsetel laminaatidel jäid elastsusmoodulid puhaste oksiidide moodulite väärtuste vahepeale, välja arvatud ZrO_2-Ta_2O_5 nanolaminaatide korral, milledel olid elastsumoodulid suuremad võrreldes puhaste koostisoksiididega. Nähtuse täpsed põhjused on veel välja selgitamata.

Kõvaduse poolest olid puhtad Al_2O_3 ja HfO_2 peaaegu 2 korda kõvemad klaasist alusest (vastavalt 11–12 GPa ja 6,7 GPa). Tsirkoonium- ja tantaaloksiid olid klaasile lähedase kõvadusega ($\approx$7 GPa).

Tulemustest saab järeldada, et ALD kiled on suhteliselt kõvad materjalid ja neid saaks sobitada erinevate materjalide elastsusmoodulitega kasutades erinevaid komposiitseid kooslusi. Viimane võib olla kasulik näiteks juhul, kui soovitakse kasutada ALD kilesid metallide või sulamite kaitsmiseks (nt korrosioonikaitse). Samuti võimaldaks ALD kilede kasutamine muuta materjalide pindade mehaanilisi omadusi, mis võib olla vajalik näiteks mikro- või nanoelektormehaaniliste seadmete (NEMS/MEMS) korral.

ACKNOWLEDGEMENTS

REFERENCES

[1]   R. W. Johnson, A. Hultqvist, S. F. Bent. A brief review of atomic layer deposition: from fundamentals to applications. Materialstoday, Vol. 17, Iss. 5 (2014) 236–246. DOI: 10.1016/j.mattod.2014.04.026.

[2]   V. Miikkulainen, M. Leskelä, M. Ritala, R. L. Puurunen. Crystallinity of inorganic films grown by atomic layer deposition: Overview and general trends. Journal of Applied Physics 113, 021301 (2013). DOI: 10.1063/1.4757907.

[3]   T. Suntola, J. Antson, A. Pakkala, S. Lindfors, SID80 Digest 11 (1980) 108.

[4]   J. H. Choi, Y. Mao, J. P. Chang. Development of hafnium based high-k materials – A review. Materials Science and Engineering R 72 (2011) 97–136.
DOI: 10.1016/j.mser.2010.12.001.

[5]   R. D. Clark. Emerging Applications for High K Materials in VLSI Technology. Materials 7 (2014) 2913–2944. DOI: 10.3390/ma7042913.

[6]   Y. Kamata. High-k/Ge MOSFETs for future nanoelectronics. Materialstoday, Vol. 11, Iss. 1–2 (2008) 30–38. DOI: 10.1016/S1369-7021(07)70350-4.

[7]   B. J. O'neill, D. H. K. Jackson, J. Lee, C. Canlas, P. C. Stair, C. L. Marshall, J. W. Elam, T. F. Kuech, J. A. Dumesic, G. W. Huber. Catalyst Design with Atomic Layer Deposition. ACS Catalysis, Vol. 5 (2015) 1804–1825.
DOI: 10.1021/cs501862h.

[8]   E. Marin, A. Lanzutti, M. Lekka, L. Guzman, W. Ensinger, L. Fedrizzi. Chemical and mechanical characterization of TiO2/Al2O3 atomic layer depositions on AISI 316 L stainless steel. Surface and Coatings Technology, Vol. 211 (2012) 84–88. DOI: 10.1016/j.surfcoat.2011.08.026.

[9]   E. Härkönen, I. Kolev, B. Diaz, J. Światowska, V. Maurice, A. Seyeux. P. Marcus, M. Fenker, L. Toth, G. Radnoczi, M. Vehkämäki, M. Ritala. Sealing of Hard CrN and DLC Coatings with Atomic Layer Deposition. ACS Applied Materials& Interfaces, Vol. 6 (2014) 1893–1901.

[10]   Hardness Testing, 2nd Edition. Editor: Harry Chandler. (ASM International, U.S.A., 1999). ISBN: 978-0-87170-640-9.

[11]   W. C. Oliver, G. M. Pharr. An improved technique for determining hardness and elastic modulus using load and displacement sensing indentation experiments. Journal of Materials Research, Vol. 7, Iss. 6 (1992). 1564–1583.
DOI: 10.1557/JMR.1992.1564.

[12]   W. C. Oliver, G. M. Pharr. Measurement of hardness and elastic modulus by instrumented indentation: Advances in understanding and refinements to methodology. Journal of Materials Research, Vol. 19, Iss. 1 (2004) 3–20.
DOI: 10.1557/jmr.2004.19.1.3.

[13]   M. G. Bader, P. Bussi, L. A. Carlsson, K. K. Chawla, R. F. Eduljee, G. Fantozzi, A. R. Hill, H.Ishida, A. Kelly, J.-K. Kim, R. Y. Kim, Y.-W. Mai, R. L. MacCullogh, G. M. Newaz, C. Olagnon, A. Parvizi-Majidi, C. T. Sun, R. Talreja. Materials Science and Technology: A Comprehensive Treatment, Vol. 13 Structure and Properties of Composites. Editors in chief: R. W. Cahn, P. Haasen, E. J. Kramer. Volume editor: T. W. Chou. (VCH Verlagsgesellschaft mbH., Federal Republic of Germany, 1993). ISBN 3-527-26813-8.

[14]   J. M. Stickel, M. Nagarajan. Glass Fiber-Reinforced Composites: From Formulation to Application. International Journal of Applied Glass Science, Vol. 3, Iss. 2 (2012) 122–136. DOI: 10.1111/j.2041-1294.2012.00090.x.

[15]   K. Yong, J. Jeong. Applications of Atomic Layer Chemical Vapor Deposition for the Processing of Nanolaminate Structures. Korean Journal of Chemical Engineering 19(3) (2002).

[16]   R. L. Puurunen. Surface chemistry of atomic layer deposition: A case study for the trimethylaluminum/water process. Journal of Applied Physics 97, 121301 (2005). DOI: 10.1063/1.1940727.

[17]   S. M. George. Atomic Layer Deposition: An Overview. Chemical Reviews, Vol. 110, No. 1 (2010). DOI: 10.1021/cr900056b.

[18]   K. L. Choy. Chemical vapour deposition of coatings. Progress in Materials Science 48 (2003). DOI: 10.1061/S0079-6425(01)00009-3.

[19]   R. Beetstra, U. Lafont, J. Nijenhuis, E. M. Kelder, J. R. van Ommen. Atmospheric Pressure Process for Coating Particles Using Atomic Layer Deposition. Chemical Vapor Deposition 15 (2009). DOI: 10.1002/cvde.200906775.

[20]   K. Kukli, M. Kemell, J. Köykkä, K. Mizohata, M. Vehkamäki, M. Ritala, M. Leskelä. Atomic layer deposition of zirconium dioxide from zirconium tetrachloride and ozone. Thin Solid Films 589 (2015). DOI: 10.1016/j.tsf.2015.06.033.

[21]   V. Miikulainen. M. Leskelä, M. Ritala, R. L. Puurunen. Crystallinity of inorganic films grown by atomic layer deposition: Overview and general trends. Journal of Applied Physics 113, 021301 (2013). DOI: 10.1063/1.4757907.

[22]   T. Hatanpää, M. Ritala, M. Leskelä. Precursors as enablers of ALD technology: Contributions from University of Helsinki. Coordination Chemistry Reviews 257 (2013). DOI: 10.1016/j.ccr.2013.07.002.

[23]   L. Hiltunen, H. Kattelus, M. Leskelä, M. Mäkelä, L. Niinistö, E. Nykänen, P Soininen, M. Tiitta. Growth and characterization of aluminium oxide thin films deposited from various source materials by atomic layer epitaxy and chemical vapor deposition processes. Materials Chemistry and Physics 28 (1991).

[24]   L. Aarik, T. Arroval, R. Rammula, H. Mändar, V. Sammelselg, B. Hudec, K. Hušeková, K. Frölich, J. Aarik. Atomic layer deposition of high-quality Al2O3 and Al-doped TiO2 thin films from hydrogen-free precursors. Thin Solid Films 565 (2014). DOI: 10.1016/j.tsf.2014.06.038.

[25]   P. Atkins, J. de Paula. Physical Chemistry for the Life Sciences. Oxford University Press, Oxford, United Kingdom (2006).

[26]   CRC Handbook of Chemistry and Physics, Internet Version 2005, http://hbcnetbase.com, CRC Press, Boca Raton, Florida, United States of America (2005).

[27]   J. Aarik, K. Kukli, A. Aidla, L. Pung. Mechanism of suboxide growth and etching in atomic layer deposition of tantalum oxide from TaCl5 and H2O. Applied Surface Scinece 103 (1996). DOI: 10.1016/S0169-4332(96)00554-5.

[28]   J. H. Han, E. Ungur, A. Franquet, K. Opsomer, T. Conard, A. Moussa, S. De Gendt, S. Van Elshocht, C. Adelmann. Atomic layer deposition of tantalum oxide and tantalum silicate from TaCl5, SiCl4 and O3: growth bevaviour and film characteristics. Journal of Material Chemistry C 1 (2013). DOI: 10.1039/c3tc31172d.

[29]   J. Lyytinen, X. Liu, O. M.E. Ylivaara, S. Sintonen, A. Iyer, S. Ali, J. Julin, H. Lipsanen. T. Sajavaara. R. L. Puurunen, J. Koskinen. Nanotribological, nanomechanical and interfacial characterization of atomic layer deposited TiO2 on silicon substrate. Wear 342–343 (2015). DOI: 10.1016/j.wear.2015.09.001.

[30] J. Aarik, A. Aidla, V. Sammelselg, T. Uustare, M. Ritala, M. Leskelä. Characterization of titanium dioxide atomic layer growth from titanium ethoxide and water. Thin Solid Films 370 (2000). DOI: 10.1016/S0040-6090(00)00911-1.

[31] D. M. Hausmann, R. G. Gordon. Surface morphology and crystallinity control in the atomic layer deposition (ALD) of hafnium and zirconium oxide thin films. Journal of Crystal Growth 249 (2003). DOI: 10.1016/S0022-0248(02)02133-4.

[32] A. C. Jones, M. L. Hitchman. Chemical Vapour Deposition: Precursors, Processes and Applications (2008). Royal Society of Chemistry, Cambridge, England.

[33] J. Aarik, A. Aidla, A. Jaek, A.-A. Kiisler, A.-A. Tammik. Properties of amorphous Al2O3 films grown by ALE. Acta Polytechnica Scandinavica (1990).

[34] J. Aarik, A. Aidla, H. Mändar, V. Sammelselg, T.Uustare. Texture development in nanocrystalline hafnium dioxide thin films grown by atomic layer deposition. Journal of Crystal Growth 220 (2000). DOI: 10.1016/S0022-0248(00)00831-9.

[35] J. Aarik, A. Aidla, K. Kukli, T. Uustare. Deposition and etching of tantalum oxide thin films in atomic layer deposition process. Journal of Crystal Growth 144 (1999). DOI: 10.1016/S0022-0248(00)00331-6.

[36] J. Aarik, A. Aidla, T. Uustare, V. Sammelselg. Morphology and structure of TiO2 thin films grown by atomic layer deposition. Journal of Crystal Growth 148 (1995). DOI: 10.1016/S0022-0248(94)00874-4.

[37] J. Aarik, A. Aidla, H. Mändar, T. Uustare, V. Sammelselg. Growth kinetics and structure formation of ZrO2 thin films in chloride-based atomic layer deposition process. Thin Solid Films 408 (2002). DOI: 10.1016/S0040-6090(02)00123-2.

[38] A. Holmqvist, T. Törngahl, F. Magnusson, U. Zimmermann, S. Stenström. Dynamic parameter estimation of atomic layer deposition kinetics applied to in situ quartz crystal microbalance diagnostics. Chemical Engineering Science 111 (2014). DOI: 10.1016/j.ces.2014.02.005.

[39] R. A. Wind, S. M. George. Quartz Crystal Microbalance Studies of Al2O3 Atomic Layer Deposition Using Trimethylaluminum and Water at 125 °C. Journal of Physical Chemistry A 114 (2010). DOI: 10.1021/jp9049268.

[40] J. F. Mack, P. B. Van Stockum, Y. T. Temane, M. Logar, H. Iwadate, F. B. Prinz. Observing the Nucleation Phase of Atomic Layer Deposition In Situ. Chemistry of Materials 24 (2012). DOI: 10.1021/cm302398v.

[41] The Hardness of Metals. Editor: D. Tabor. (Oxford University Press Inc., U.S.A., 2000). ISBN: 0-19-850776-3.

[42] M. F. Doerner, W. D. Nix. A method for interpreting the data from depth-sensing indentation instruments. Journal of Materials Research, Vol. 1, Iss. 4, 601–609 (1986). DOI: 10.1557/JMR.1986.0601.

[43] M. R. VanLandingham. Review of Instrumented Indentation. Journal of Research of the National Institute of Standards and Technology, Vol. 108, Iss. 4, 249–265 (2003).

[44] I. N. Sneddon. The relation between load and penetration in the axisymmetric Boussinesq problem for a punch of arbitrary profile. International Journal of Engineering Science, Vol. 3, 47–57.

[45] X. Li, B. Bhushan. A review of nanoindentation continuous stiffness measurement technique and its applications. Materials Characterization, Vol. 48, 11–36 (2002). DOI: 10.1016/S1044-5803(02)00192-4.

[46] G. Guillonneau, G. Kermouche, S. Bec, J.-L. Loubet. Determination of mechanical properties by nanoindentation independently of indentation depth measurement.

Journal of Materials Research, Vol. 27, 2551–2560 (2012).
DOI: 10.1557/jmr.2012.261.

[47] R. M. Christensen. Mechanics of Composite Materials. (Dover Publications, Inc., U. S. A., 2005). ISBN 0-486-44239-X.

[48] W. Voigt. Ueber die Beziehung Zwischen den beiden Elasticitätsconstanten isotroper Körper. Annalen der physic, Vol. 274, Iss. 12 (1889).
DOI: 10.1002/andp.18892741206.

[49] A. Reuss. Berechnung der Fließgrenze von Mischkristallen auf Grund der Plastizitätsbedingung für Einkristalle. Zeitschrift für Angewandte Mathematik und Mechanik, Vol. 9, Iss. 1 (1929). DOI: 10.1002/zamm.19290090104.

[50] J. E. Ashton, J. C. Halpin, P. H. Petit. Primer on Composite Materials: Analysis. 1st Edition. Technomic Publishing Company Inc., Pennsylvania, U.S.A., (1969). ISBN: 0-87762-754-1.

[51] J. C. Halpin, S. W. Tsai. Air Force Technical Report AFML-TR-67-423 (1969).

[52] J. C. Halpin. Primer on Composite Materials Analysis. 2nd Edition. CRC Press, ISBN: 978-0877627548.

[53] R. L. Foye. The transverse Poisson's Ratio of Composites. Journal of Composite Materials. Vol. 6, Iss. 2, 293–295 (1972, online published 2016).
DOI: 10.1177/002199837200600209.

[54] T. B. Lewis, L. E. Nielsen. Dynamic mechanical properties of particulate-filled composites. Journal Applied Polymer Science, Vol. 14, Iss. 6, 1449–1471 (1970).
DOI: 10.1002/app.1970.070140604.

[55] S. H. McGee, R. L. McCullough. Combining rules for predicting the thermo-elastic properties of particulate filled polymers, polymers, polyblends, and foams. Polymer Composites, Vol. 2, Iss. 4 149–161 (1981). DOI:10.1002/pc.750020403.

[56] E. A. Dean, J. A. Lopez. Empirical Dependence of Elastic Moduli on Porosity for Ceramic Materials. Journal of American Ceramic Society, Vol. 66, Iss. 5, 366–370 (1983). DOI: 10.1111/j.1151-2916.1983.tb10051.x.

[57] L. Zhang, J. H. Prosser, G. Feng, D. Lee. Mechanical properties of atomic layer deposition-reinforced nanoparticle thin films. Nanoscale 4 (2012).
DOI: 10.1039/c2nr32016a.

[58] A. K. Roy, W. Baumann, S. Schulze, M. Hietschold, T. Mäder, D. J. Nestler, B. Wielage, W. A. Goedel. Atomic layer Deposition of alumina onto carbon fibers. Journal of American Cermic Society 94, Issue 7 (2011).
DOI: 10.1111/j.1551-2916.2010.04342.x.

[59] B. Matovic, F. Zivic, S. Mitrovic, D. Prsic, V. Maksimovic, T. Volkov-Husovic, R. Kumar, N. Daneu. Ultra-high pressure densification and properties of nano-structured SiC. Material Letters 164 (2016). DOI: 10.1016/j.matlet.2015.09.043.

[60] O. M. E. Ylivaara, X. Liu, L. Kilpi, J. Lyytinen, D. Schneider, M. Laitinen, J. Julin, S. Ali, S. Sintonen, M. Berdova, E. Haimi, T. Sajavaara, H. Ronkainen, H. Lipsanen, J. Koskinen, S.-P. Hannula, R. L. Puurunen. Aluminum oxide from trimethylaluminum and water by atomic layer deposition: The temperature dependence of residual stress, elastic modulus, hardness and adhesion. Thin Solid Films 552 (2014) 124–135. DOI: 10.1016/j.tsf.2013.11.112.

[61] K. Kukli, J. Ihanus, M. Ritala, M. Leskelä. Properties of Ta2O5-Based Dielectric Nanolaminates Deposited by Atomic Layer Epitaxy. Journal of The Electro-chemical Society, Vol. 144, Iss. 1, 300–306 (1997). DOI:10.1149/1.1837399.

[62]   K.Kukli, J. Ihanus, M. Ritala, M. Leskelä. Tailoring the dielectric properties of HfO2-Ta2O5 nanolaminates. Applied Physics Letters, Vol. 68, No. 26, 3737–3739 (1996). DOI:10.1063/1.115990.

[63]   B. Aitken, A. Atkinson, S. P. S. Badwal, G. H. Beall, P. F. Becher, R. Brezny, J. D. Cawley, D. R. Clarke, R. F. Cook, M. Daumling, B. B. Ghate, A. Goldman, D. J. Green, S. Hampshire, B. G. Hyde, K. Komeya, W. E. Lee, M. Matsui, G. M. Pharr, G. E. Pike, F. Rose, R. Telle, J. G. Thompson, K. Uchino, R. L. Withers. Materials Science and Technology: A Comprehensive Treatment, Vol. 11 Structure and Properties of Ceramics. Editors in chief: R. W. Cahn, P. Haasen, E. J. Kramer. Volume editor: M. Swain. (VCH Verlagsgesellschaft mbH., Federal Republic of Germany, 1994). ISBN 3-527-26813-8.

[64]   R. H. J. Hannik, P. M. Kelly, B. C. Muddle. Transformation Toughening in Zirconia-Containing Ceramics. Journal of the American Ceramic Society, Vol. 83, Iss. 3 (2000). DOI: 10.1111/j.1151-2916.2000.tb01221.x.

[65]   E. S. Puchi-Gabrera. A new model for the computational of the composite hardness of coated systems. Surface and Coatings Technology 160, 177–186 (2002). DOI: 10.1016/S0257-8972(02)00394-8.

[66]   J. R. Tuck, A. M. Korsunsky, S. J. Bull. Surface and Coatings Technology, Vol. 127 (2000). DOI:10.1016/S0257-8972(00)00537-5.

[67]   I. Manika, J. Maniks. Effect of substrate hardness and film structure on indentation depth criteria for film hardness testing. Journal of Physics D: Applied Physics, Vol. 41, 074010, 1–6 (2008). DOI: 10.1088/0022-3727/41/7/07/4010.

[68]   E. S. Puchi-Cabrera. A new model for the computation of the composite hardness of coated systems. Surface and Coatings Technology, Vol. 160, 177–186, 2002. DOI: 10.1016/jS0257-8972(02)00394-8.

[69]   J. Menčík. Nanoindentation in Materials Science, Uncertainties and Errors in Nanoindentation. Editor in chief: J. Nemecek, InTech (2012). DOI:10.5772/50002.

PUBLICATIONS

CURRICULUM VITAE

Name   Taivo Jõgiaas
Date of birth   6.05.1981
E-mail   taivo.jogiaas@ut.ee

Institution and position

01.01.2016–31.12.2018	University of Tartu, Faculty of Science and Technology, Institute of Physics, Engineer (1,00)
01.10.2015–31.12.2015	University of Tartu, Faculty of Science and Technology (old), Institute of Physics, University of Tartu, Engineer (1,00)
2014–31.12.2014	University of Tartu, Other staff (0,50)
24.06.2013–31.12.2014	University of Tartu, Faculty of Science and Technology (old), Institute of Physics, University of Tartu, Engineer (0,50)

Education

2012–...	University of Tartu, Doctor of Philosophy, Materials Science
2010–...	University of Tartu, Master of Science, Materials Science
1999–...	University of Tartu, Bachelor of Science, Materials Science
1996–...	Rõngu High School

Academic degrees

Taivo Jõgiaas, Master's Degree, 2012, (sup) Ants Lõhmus; Rünno Lõhmus, Pilootprojekt kiiresti liikuvate mikroosakeste suuruse ja kuju visuali-seerimiseks (The pilot project for visualizing size and shape of fast moving microparticles), University of Tartu.

Taivo Jõgiaas, Phd student, (sup) Irina Hussainova; Kaupo Kukli; Aile Tamm, Nanoparticles modified by atomic layer deposition for high performance composites, University of Tartu.

Projects in progress

TK134 "Kontrollitud korrastatus kvant- ja nanomaterjalides (1.01.2016−1.03.2023)", Aile Tamm, Tartu Ülikool, Loodus- ja täppisteaduste valdkond, Füüsika instituut.

IUT2-24 "Kilestruktuurid nanoelektroonika rakendusteks ja funktsionaalseteks pinnakateteks (1.01.2013−31.12.2018)", Väino Sammelselg, Tartu Ülikool, Loodus- ja täppisteaduste valdkond, Füüsika instituut.

Publications

3.4/2017

Uudeküll, P.; Jõgiaas, T.; Kozlova, J.; Klaas, M.; Link, J.; Stern, R.; Tätte, T.; Jaks, V.; Tamm, A. (2017). Atomic Layer Deposition of Titanium Oxide Films on As-Synthesized Magnetic Metal (Oxide) Nanoparticles. *Baltic ALD2015, The 13th International Baltic Conference on Atomic Layer Deposition, Tartu, Estonia, 28,29 September,2015*.

5.2/2017

Jõgiaas, Taivo; Zabels, Roberts; Tamm, Aile; Hussainova, Irina; Heikkilä, Mikko; Mändar, Hugo; Kozlova, Jekaterina; Kukli, Kaupo; Ritala, Mikko; Leskelä, Markku. (2017). Mechanical properties of aluminium, zirconium, hafnium and tantalum oxides and their nanolaminates grown by atomic layer deposition. *Baltic ALD 2015, Tartu, Estonia*.

1.1/2016

Kukli, Kaupo; Salmi, Emma; Jõgiaas, Taivo; Zabels, Roberts; Schuisky, Mikael; Westlinder, Jörgen; Mizohata, Kenichiro; Ritala, Mikko; Leskelä, Markku (2016). Atomic layer deposition of aluminum oxide on modified steel substrates. *Surface & Coatings Technology, 304, 1−8, 10.1016/j.surfcoat.2016.06.064*.

3.4/2016

Jõgiaas, Taivo; Zabels, Roberts; Seemen, Helina; Tamm, Aile; Kukli, Kaupo (2016). Atomic layer deposited thin films with gradient composition. *ALD 2016, the 16th International Conference on Atomic Layer Deposition, Dublin, Ireland, 24–27 July 2016*.

3.4/2016

Seemen, Helina; Jõgiaas, Taivo; Tamm, Aile; Sammelselg, Väino (2016). The formation and distribution of cracks in bent atomic layer deposited coatings. *ALD 2016, the 16th International Conference on Atomic Layer Deposition, Dublin, Ireland, 24–27 July 2016*.

5.2/2016

Seemen, Helina; Jõgiaas, Taivo; Kibur, Ragnar-Toomas (2016). Using Atomic Layer Deposition for Microtome Blade Cutting Performance Enhancement. *Baltic ALD2015, The 13th International Baltic Conference on Atomic Layer Deposition, Tartu, Estonia, 28, 29 September, 2015*.

1.1/2015

Jõgiaas, T.; Kollo, L.; Kozlova, J.; Tamm, A.; Hussainova, I.; Kukli, K. (2015). Effect of Atomic Layer Deposited Aluminium Oxide on Mechanical Properties of Porous Silicon Carbide. *Ceramics International, 41 (6), 7519−7528, 10.1016/j.ceramint.2015.02.074.*

1.1/2015

Jõgiaas, T.; Zabels, R.; Tamm, A.; Merisalu, M.; Hussainova, I.; Heikkilä, M.; Mändar, H.; Kukli, K.; Ritala, M.; Leskelä, M. (2015). Mechanical properties of aluminium, zirconium, hafnium and tantalum oxides and their nanolaminates grown by atomic layer deposition. *Surface & Coatings Technology, 282, 36−42, 10.1016/j.surfcoat.2015.10.008.*

1.1/2014

Jõgiaas, T.; Arroval, T.; Kollo, L.; Kozlova, J.; Käämbre, T.; Mändar, H.; Tamm, A.; Hussainova, I.; Kukli, K. (2014). Atomic layer deposition of alumina on γ-Al2O3 nanofibers. *Physica Status Solidi A – Applications and Materials Science, 211 (2), 403−408, dx.doi.org/10.1002/pssa.201330083.*

6.7/2014

Jõgiaas, Taivo; Kozlova, Jekaterina; Arroval, Tõnis; Käämbre, Tanel; Mändar, Hugo; Kollo, Lauri; Tamm, Aile; Hussainova, Irina, Kukli, Kaupo (2014). Atomic Layer Deposition for Hard Nanocoatings. *Baltic ALD 2014: Baltic ALD 2014 12th International Baltic Conference on Atomic Layer Deposition, May 12–13, 2014, Helsinki, Finland.*

ELULOOKIRJELDUS

Nimi	Taivo Jõgiaas
Sünniaeg	6.05.1981
E-post	taivo.jogiaas@ut.ee

Töökohad ja ametid

01.01.2016–31.12.2018	Tartu Ülikool, Loodus- ja täppisteaduste valdkond, Füüsika instituut, insener (1,00)
01.10.2015–31.12.2015	Tartu Ülikool, Loodus- ja tehnoloogiateaduskond, Tartu Ülikooli Füüsika Instituut, insener (1,00)
2014–31.12.2014	Tartu Ülikool, Muu töö (0,50)
24.06.2013–31.12.2014	Tartu Ülikool, Loodus- ja tehnoloogiateaduskond, Tartu Ülikooli Füüsika Instituut, insener (0,50)

Haridustee

2012–...	Tartu Ülikool, doktoriõpe, materjaliteadus
2010–...	Tartu Ülikool, magistriõpe, materjaliteadus
1999–...	Tartu Ülikool, bakalaureuseõpe, materjaliteadus
1996–...	Keskharidus, Rõngu Keskkool

Teaduskraadid

Taivo Jõgiaas, magistrikraad, 2012, (juh) Ants Lõhmus; Rünno Lõhmus, Pilootprojekt kiiresti liikuvate mikroosakeste suuruse ja kuju visualiseerimiseks, Tartu Ülikool.

Taivo Jõgiaas, doktorant, (juh) Irina Hussainova; Kaupo Kukli; Aile Tamm, Nanoparticles modified by atomic layer deposition for high performance composites (Aatomkihtsadestamisega modifitseeritud nanoosakeste mõju uudsete komposiitide omadustele), Tartu Ülikool.

Jooksvad projektid

TK134 "Kontrollitud korrastatus kvant- ja nanomaterjalides (1.01.2016−1.03.2023)", Aile Tamm, Tartu Ülikool, Loodus- ja täppisteaduste valdkond, Füüsika instituut.

IUT2-24 "Kilestruktuurid nanoelektroonika rakendusteks ja funktsionaalseteks pinnakateteks (1.01.2013−31.12.2018)", Väino Sammelselg, Tartu Ülikool, Loodus- ja täppisteaduste valdkond, Füüsika instituut.

Publikatsioonid

3.4/2017

Uudeküll, P.; Jõgiaas, T.; Kozlova, J.; Klaas, M.; Link, J.; Stern, R.; Tätte, T.; Jaks, V.; Tamm, A. (2017). Atomic Layer Deposition of Titanium Oxide Films on As-Synthesized Magnetic Metal (Oxide) Nanoparticles. *Baltic ALD2015, The 13th International Baltic Conference on Atomic Layer Deposition, Tartu, Eesti, 28–29 september,2015.*

5.2/2017

Jõgiaas, Taivo; Zabels, Roberts; Tamm, Aile; Hussainova, Irina; Heikkilä, Mikko; Mändar, Hugo; Kozlova, Jekaterina; Kukli, Kaupo; Ritala, Mikko; Leskelä, Markku. (2017). Mechanical properties of aluminium, zirconium, hafnium and tantalum oxides and their nanolaminates grown by atomic layer deposition. *Baltic ALD 2015, Tartu, Eesti.*

1.1/2016

Kukli, Kaupo; Salmi, Emma; Jõgiaas, Taivo; Zabels, Roberts; Schuisky, Mikael; Westlinder, Jörgen; Mizohata, Kenichiro; Ritala, Mikko; Leskelä, Markku (2016). Atomic layer deposition of aluminum oxide on modified steel substrates. *Surface & Coatings Technology, 304, 1−8, 10.1016/j.surfcoat.2016.06.064.*

3.4/2016

Jõgiaas, Taivo; Zabels, Roberts; Seemen, Helina; Tamm, Aile; Kukli, Kaupo (2016). Atomic layer deposited thin films with gradient composition. ALD 2016, the 16th International Conference on Atomic Layer Deposition, Dublin, Iirimaa, 24–27 juuli 2016.

3.4/2016

Seemen, Helina; Jõgiaas, Taivo; Tamm, Aile; Sammelselg, Väino (2016). The formation and distribution of cracks in bent atomic layer deposited coatings. *ALD 2016, the 16th International Conference on Atomic Layer Deposition, Dublin, Iirimaa, 24–27 juuli 2016.*

5.2/2016

Seemen, Helina; Jõgiaas, Taivo; Kibur, Ragnar-Toomas (2016). Using Atomic Layer Deposition for Microtome Blade Cutting Performance Enhancement. *Baltic ALD2015, The 13th International Baltic Conference on Atomic Layer Deposition, Tartu, Eesti, 28–29 september, 2015.*

1.1/2015

Jõgiaas, T.; Kollo, L.; Kozlova, J.; Tamm, A.; Hussainova, I.; Kukli, K. (2015). Effect of Atomic Layer Deposited Aluminium Oxide on Mechanical Properties of Porous Silicon Carbide. *Ceramics International, 41 (6), 7519−7528, 10.1016/j.ceramint.2015.02.074.*

1.1/2015

Jõgiaas, T.; Zabels, R.; Tamm, A.; Merisalu, M.; Hussainova, I.; Heikkilä, M.; Mändar, H.; Kukli, K.; Ritala, M.; Leskelä, M. (2015). Mechanical properties of aluminium, zirconium, hafnium and tantalum oxides and their nanolaminates grown by atomic layer deposition. *Surface & Coatings Technology, 282, 36−42, 10.1016/j.surfcoat.2015.10.008.*

1.1/2014

Jõgiaas, T.; Arroval, T.; Kollo, L.; Kozlova, J.; Käämbre, T.; Mändar, H.; Tamm, A.; Hussainova, I.; Kukli, K. (2014). Atomic layer deposition of alumina on γ-Al2O3 nanofibers. *Physica Status Solidi A – Applications and Materials Science, 211 (2), 403−408, dx.doi.org/10.1002/pssa.201330083.*

6.7/2014

Jõgiaas, Taivo; Kozlova, Jekaterina; Arroval, Tõnis; Käämbre, Tanel; Mändar, Hugo; Kollo, Lauri; Tamm, Aile; Hussainova, Irina, Kukli, Kaupo (2014). Atomic Layer Deposition for Hard Nanocoatings. *Baltic ALD 2014: Baltic ALD 2014 12th International Baltic Conference on Atomic Layer Deposition, 12–13 mai, 2014, Helsinki, Soome.*

DISSERTATIONES SCIENTIAE MATERIALIS
UNIVERSITATIS TARTUENSIS